Chemistry and Physics of Lipids 219 (2019) 1–14

Contents lists available at ScienceDirect

Chemistry and Physics of Lipids

journal homepage: www.elsevier.com/locate/chemphyslip

Imaging with mass spectrometry, the next frontier in sphingolipid research? A discussion on where we stand and the possibilities ahead

Chiara Luberto[a,*], John D. Haley[b], Maurizio Del Poeta[c,d,e,f]

[a] Department of Physiology and Biophysics, Stony Brook University, Stony Brook, NY, United States
[b] Department of Pathology, Stony Brook University, Stony Brook, NY, United States
[c] Department of Molecular Genetics and Microbiology, Stony Brook University, Stony Brook, NY, United States
[d] Division of Infectious Diseases, Stony Brook University, Stony Brook, NY, United States
[e] Institute of Chemical Biology and Drug Discovery, Stony Brook University, Stony Brook, NY, United States
[f] Veterans Administrations Medical Center, Northport, NY, United States

ARTICLE INFO

Keywords:
Mass spectrometry imaging
MSI
Matrix-assisted laser desorption ionization
MALDI
Secondary ion mass spectrometry
SIMS
Desorption electrospray ionization
DESI
Sphingolipids
Ceramide
Sphingomyelin
Ceramide-1-phosphate
Sphingosine-1-phosphate

ABSTRACT

In the last ten years, mass spectrometry (MS) has become the favored analytical technique for sphingolipid (SPL) analysis and measurements. Indeed MS has the unique ability to both acquire sensitive and quantitative measurements and to resolve the molecular complexity characteristic of SPL molecules, both across the different SPL families and within the same SPL family. Currently, two complementary MS-based approaches are used for lipid research: analysis of *lipid extracts,* mainly by infusion electrospray ionization (ESI), and mass spectrometry imaging (MSI) from a sample surface (i.e. *intact* tissue sections, cells, model membranes, thin layer chromatography plates) (Fig. 1). The first allows for sensitive and quantitative information about total lipid molecular species from a given specimen from which lipids have been extracted and chromatographically separated prior to the analysis; the second, albeit generally less quantitative and less specific in the identification of molecular species due to the complexity of the sample, allows for spatial information of lipid molecules from biological specimens. In the field of SPL research, MS analysis of lipid extracts from biological samples has been commonly utilized to implicate the role of these lipids in specific biological functions. On the other hand, the utilization of MSI in SPL research represents a more recent development that has started to provide interesting descriptive observations regarding the distribution of specific classes of SPLs within tissues. Thus, it is the aim of this review to discuss how MSI technology has been employed to extend the study of SPL metabolism and the type of information that has been obtained from model membranes, single cells and tissues. We envision this discussion as a complementary compendium to the excellent technical reviews recently published about the specifics of MSI technologies, including their application to SPL analysis (Fuchs et al., 2010; Berry et al., 2011; Ellis et al., 2013; Eberlin et al., 2011; Kraft and Klitzing, 2014).

1. Introduction

Visualization of sphingolipids (SPLs) and of lipids in general is an approach to biological studies that has recently attracted much attention. Indeed, as we begun to appreciate the importance of the compartmentalized nature of SPL metabolism and signaling within cells, the need to specifically visualize the spatial origin of the lipid signal within cells became critical (Hannun and Obeid, 2018; Ogretmen, 2018; Pyne et al., 2018; Newton et al., 2015). Moreover, when considering the complexity and the diversity of tissue samples, it is apparent that crude lipid measurements from whole tissue extracts are a superficial way to associate lipid changes to specific morphological traits. A limited SPL-imaging tool set was at first available, counting mainly on semispecific antibodies (i.e. for ceramide and sphingomyelin (SM)) and on lipid binding proteins for indirect probing. As the advent of mass spectrometry (MS) allowed the precise identification and quantitation of sphingolipid molecules (Sullards et al., 2011; Farwanah et al., 2011), the development of MS-based visualization approaches followed.

2. General considerations for imaging lipids by MS

Mass spectrometry imaging (MSI) for lipids has been most commonly obtained using three different systems: matrix-assisted laser desorption ionization (MALDI) (Hillenkamp et al., 1991), secondary ion

* Corresponding author at: Department of Physiology and Biophysics Stony Brook University, Stony Brook, United States.
E-mail address: Chiara.luberto@stonybrook.edu (C. Luberto).

https://doi.org/10.1016/j.chemphyslip.2019.01.001
Received 27 September 2018; Received in revised form 2 January 2019; Accepted 3 January 2019
Available online 11 January 2019
0009-3084/

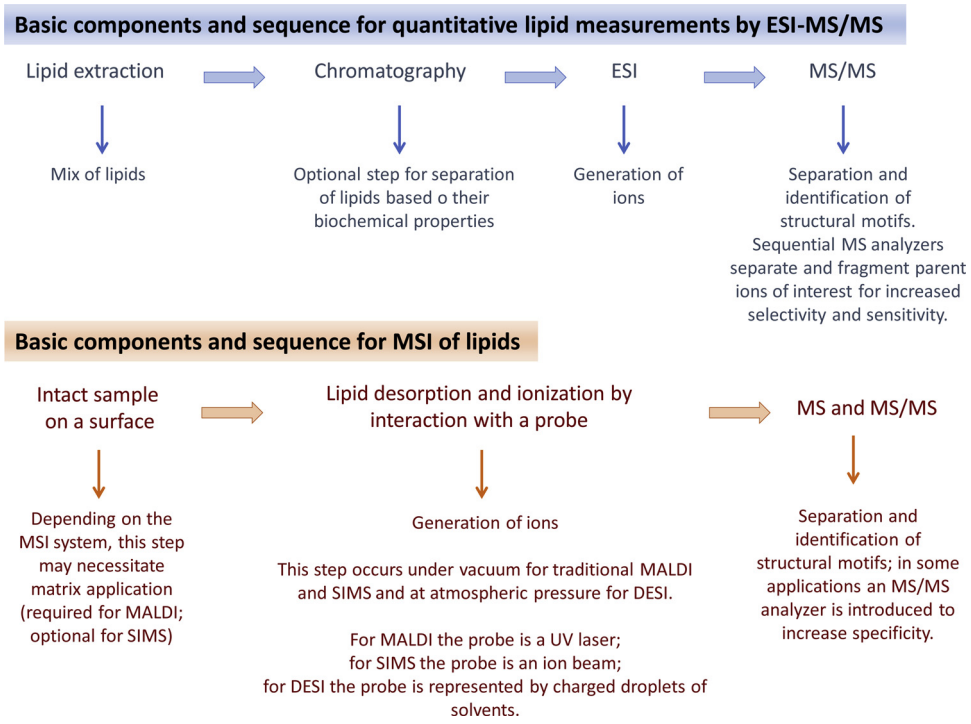

Fig. 1. Schematic representations of the basic components required for quantitative analysis of lipids by ESI-MS/MS and for lipid MSI. In blue are the components for the generation of lipid ions by ESI-MS/MS and in red are the components for the generation of lipid ions for MSI analysis. ESI: electrospray ionization.

mass spectrometry (SIMS) and desorption electrospray ionization (DESI). The first two techniques, in their traditional set up, have the lipid desorption and ionization steps performed under vacuum while, for DESI, the analysis occurs at ambient conditions (Ellis et al., 2013).

In general terms, the biological material to be analyzed is ionized by laser desorption, electrospray ionization or by electron impact (depending on the specific MS system) (Fig. 1) to liberate characteristic positively or negatively charged ionized fragments or intact molecules of analytes of interest from the biological material. The exact identification of the ionized fragments/molecules (peak assignment) which are characterized by a specific mass-to-charge ratio (m/z), is achieved with accurate mass measurements and fragmentation analysis (often acquired by collision induced dissociation, CID) generally performed separately from the image acquisition.

The imaging component of the MS analysis is obtained by first integrating the spectral signal for a specific analyte of interest (specific mass to charge ratio, m/z) with the corresponding area on the sample that was analyzed, then converting the intensity of the spectral signal into a false color scale and overlaying the color onto the analyzed area within the sample. By repeating these steps to adjacent discrete areas in a raster pattern, a 2-D color image representing the local variation of the levels of the specific analyte on the sample is produced.

In general, while lipid molecules can be analyzed by MSI, the differences in the ionization efficiency, the hydrophobic nature of the analyte, the competitive ion suppression effects, and the differences in the efficiency of fragmentation render the comparison among different types of lipids (and sometime even for the same lipid between different tissues) challenging. However, it is assumed that, for the same lipid or closely related lipid molecules, the peak intensity approximates the differences in intrinsic concentrations (Dill et al., 2009a; Manicke et al., 2009; Wu et al., 2010).

To assist with the peak assignment, two metabolome databases, METLIN (https://metlin.scripps.edu) and LIPID MAPS (http://www.lipidmaps.org), can be utilized to cross reference masses of precursor ions (m/z). These databases are critical in assigning parent ion masses and fragment ion masses for identification. In addition, control standards can be spiked into the matrix to improve quantitation and the areas under the curve of parent ion and fragment ion peaks for lipids of interest relative to the chemically related standards would provide more accurate quantitation.

Finally, as for other imaging techniques like microscopy, statistical tools for data analysis are an essential component of the unbiased interpretation of the differences in the spectra generated by MSI. Multivariate analysis is used to resolve the complexity of the potentially large amount of data obtained. For instance, the principal component analysis (PCA) is applied to identify variables (i.e. analytes) that can best differentiate two samples (i.e. normal and tumor tissue) while k-mean generates similarity groups (clusters) among the data points (Alexandrov, 2012).

3. MSI under vacuum conditions

3.1. MALDI-MSI

MALDI is the most popular MSI method applied so far to image SPLs. In fact MALDI represents a middle ground among MSI techniques when considering resolution, sensitivity and ease of use. Two general aspects characterize MALDI analysis: the sample (i.e. tissue section) is coated with a matrix to form matrix-analyte co-crystals and the lipids in the sample are desorbed and ionized by UV laser (probe) (Fig. 1) (Fuchs et al., 2010). In particular, once hit by the laser, the matrix-analyte co-crystals vaporize, carrying intact analyte molecules into the vapor phase and exchanging ions to form charged analyte molecules. The application of the matrix onto the samples has two main functions. Firstly, the excess matrix absorbs most of the energy of the laser, thus reducing excessive fragmentation of the sample and ensuring “soft” ionization and production of ions with high mass-to-charge ratios (m/z 500–20,000) (Touboul et al., 2011; van Remoortere et al., 2010; Luxembourg et al., 2003). Secondly, the matrix facilitates the extraction of individual analytes from the samples. This is important because the smaller the matrix-analyte co-crystal, the higher the spatial resolution. However the presence of the matrix onto the sample causes the

production of background ions that, in case of detection of low molecular weight lipids such as fatty acids (FFA) substantially complicates the analysis by traditional MALDI.

For all these considerations, the coating process of the sample with matrix prior to its exposure to the laser (which includes the preparation of the sample prior to the application of the matrix, the type of matrix and method of application of the matrix to ensure homogeneous coating) is a key step for the reliability and precision of this method and it is complicate and time consuming (Murphy et al., 2011). As the analysis occurs under vacuum, another key consideration is the preservation of the sample under this condition to avoid the risk of artifactual results.

MALDI analysis can be performed in positive or negative mode, which represents the charge of the ions (cations and anions) produced from the analyte of interest. Cations and anions are generated by addition or abstraction of hydrogen or metals (i.e. Na or K) depending on the matrix employed and the type of analyte to be assessed. The rule of thumb is that an acidic matrix will generate positive ions (cations) while neutral or basic matrices generate negative ions (anions); however the presence of salts in the samples can contribute to the formation of positive ions from neutral matrices as well. Currently, the most commonly used UV absorbing matrices are 2,5-dihydroxybenzoic acid (DHB) for positive mode and 9-aminoacridine (9-AA) for negative mode. Importantly new matrices, new strategies for the application of the matrix and the addition of matrix modifiers are continuously tested and reported to better the analysis of the specific lipids of interest. SPLs have been analyzed in both positive and negative ion modes. Generally, sphingomyelin (SM) is better detected in positive mode as it is naturally positively charged. However, because of its high abundance, SM can mask less represented SPLs due to ion suppression, making a single acquisition experiment for the analysis of different SPLs potentially challenging (Petkovic et al., 2001). It is important to stress that the efficiency of ionization of a given lipid is function of many factors like the ion chemistry in the environment of the sample, the structure of the tissue, the content of water and salt, and the extend to which the analyte is desorbed (Berry et al., 2011). Thus, the amount of lipid ions generated in the sample from a specific lipid class (which visually translates into the intensity of the signal) does not necessarily correspond to the actual levels present in the sample and, as already pointed out earlier, it should be rather considered in relative terms and not compared across lipid classes (Lohmann et al., 2010). An example of these issues is represented by the discrepancy between the levels of SM and PC as measured by MALDI versus LC–MS in the brain. In fact MALDI MSI in positive ion mode showed a much higher signal for PC as compared to SM while LC–MS measurements of the same region showed comparable levels (Hankin and Murphy, 2010). Since an equimolar mixture of PC and SM in the matrix yielded similar or higher signal for SM than PC, depending on the ion mode and matrix used (Eibisch and Schiller, 2011), the lower detection of SM by MALDI in the tissue must be due to the chemical complexity of the biological sample and warns to use caution when extrapolating absolute quantification data to compare different classes of lipids (Berry et al., 2011). Recent technical developments have also aimed at increasing the extent of ionization of the sample to improve the level of information obtained. Typically, an average of less than 1 in 1000 desorbed molecules from a tissue is ionized during the first step of the analysis presenting a general problem in the overall effectiveness of capturing a comprehensive picture of the sample (Soltwisch et al., 2015). While single and multiphoton laser ionization of neutral gas phase molecules and ESI have been implemented to address and improve this shortcoming, recently the use of a second beam of a pulsed UV laser applied to the particle plume desorbed by the MALDI laser under cooling gas environment was also reported (MALDI-2) (Soltwisch et al., 2015). With this modification, a notable gain in detection, especially for less abundant lipids was recorded both in positive and negative ion modes and impressive contrast images were captured at 5um resolution. For optimal detection, the gas pressure, the time delay between pulses of the secondary laser and the energy and wavelength of the secondary lasers are all parameters that need to be specifically tuned.

Gangliosides, sulfatides or ceramide-1-phosphate (C1P) are usually detected in negative mode (even if the use of gold nanoparticles has been reported to facilitate the analysis of cerebrosides in positive mode) (Jackson et al., 2007), making a strong case that generally the complementation between analyses in both positive and negative modes represents a better strategy to acquire a more extensive and detailed lipid profile. Interestingly, novel MS imaging systems have been also reported to allow the simultaneous analysis of the same spot in both positive and negative mode facilitating the acquisition of a complete lipid panel (Korte and Lee, 2013; Kaya et al., 2017a).

The diameter of the laser beam (together with the space between individual ablated spots) ultimately determines the spatial resolution of the analysis and reported diameters typically span from 10 to 100um with a sampling depth generally in the micron range. Spatial resolution down to 1um has also been reported for imaging of proteins (Zavalin et al., 2015) while for lipids the max resolution reported was of 5um (Soltwisch et al., 2015; Zavalin et al., 2014). An important consideration though is that the higher the lateral resolution, the higher the number of pixels which means more time is needed for image acquisition. For instance, a 1 cm^2 tissue section imaged at 100 µm spatial resolution requires a 10,000 pixel image, whereas the same area imaged at 10 µm spatial resolution results in a 1,000,000 pixel image. This means that for larger samples, like large tissues areas, typical spectral acquisition rates (˜2000 to ˜7000 pixels/hour) with a traditional MALDI MSI set up can take many hours or days for analysis (Prentice et al., 2016).

Most recently, MALDI has become more accessible for routine and rapid clinical use through the development of matrix precoated glass slides, which greatly increases throughput in sample preparation (Yang and Caprioli, 2013). Different MALDI modifications have been employed for lipid imaging and among the most commonly used are MALDI-time-of-flight (TOF), Atmospheric (AP)-MALDI and Fourier Transform Ion Cyclotron Resonance (FTICR)-MALDI.

With MALDI-TOF, the addition of the TOF component enables better separation of the molecular ions. In fact, after the ions are formed, accelerated and passed through a charged grid, they drift freely through a field free space to reach the detector with a time that is inversely proportional to the square root of their mass (smaller ions travel the fastest) (Fuchs et al., 2010). Furthermore, the addition of a reflector, changing the direction of the ion beam, can dramatically improve mass resolution. As lipid analysis by MALDI often exploits instruments that are usually used for protein studies, it is common to find the MALDI combined with a “TOF” mass analyzer, which on the other hand, is not absolutely required for lipid analysis. Recently, also a MALDI-TOF/TOF instrument with continuous rastering has been shown to increase by 8–14 fold the analysis time compared to other MS/MS instrumentation greatly facilitating the measurements in larger samples (Prentice et al., 2016). An important advantage of MALDI-TOF/TOF instruments is the ability to generate fragment ion spectra to identify fatty acid chain composition.

AP-MALDI is characterized by the desorption/ionization step occurring at ambient pressure preceding the transfer of the ions into the mass spectrometer. Several advantages can be pinpointed with this modification. First, this set up is more user friendly as the sample is of easier access to the operator, allowing more high throughput applications. Second, AP-MALDI allows the cooling of the ions which ensures less fragmentation than traditional MALDI; and third, it allows the use of matrices and the analysis of samples that are not stable under vacuum and cannot be employed in traditional MALDI. On the other hand, loss of ions en route to the mass spectrometer reduces the sensitivity with respect to traditional MALDI.

FTICR mass spectrometers allow high resolution as they have high mass accuracy (< 1 ppm) which significantly increases the number of

biomolecules that can be imaged, and they have high sensitivity (attomole-femtomole concentrations). These characteristics are particularly important when analyzing complex samples (like tissues) where there are likely to be nearly-isobaric species that have very close to equal *m/z* values and cannot be easily discriminated and lipids of interest at low concentrations.

3.2. Secondary ion mass spectrometry (SIMS)-MSI

In the case of SIMS, the probe is represented by an ion beam that strikes the sample (typically mounted onto steel, glass or silicon supports) under ultra-high vacuum, causing the release of secondary ions (Fig. 1) (Kraft and Klitzing, 2014). The ion beam can focus down to 100 nm reaching a level of resolution far greater than MALDI, even though most SIMS applications work with beam sizes at around 200 nm to balance resolution and sensitivity. However, the biggest limitation with this method for lipid analysis of tissues and cells is to right tune the energy of the ion beam. In fact, the high energy of the beam generally produces extensive molecular fragmentation (meaning that the ions liberated represent fragments of the targeted molecules), causing the reduction of the mass of the ions released and therefore lowering the specificity of the signal; however too low energy will not produce sufficient secondary ions able to gain resolving information. Another problematic aspect of SIMS is the current lack of tandem mass spectrometry capabilities; however it seems that this aspect might be resolved in the near future (Fisher et al., 2016; Passarelli et al., 2017). Typically, the depth of the analysis through the sample allowed by SIMS is shallow limiting data acquisition to the surface of the sample analyzed. However by repeated hit to the same location, it is also possible to acquire information at progressively deeper levels through the sample.

For MSI of lipids, two types of SIMS have been mostly employed: TOF- and high resolution magnetic sector SIMS (or NanoSIMS). TOF-SIMS generally uses a pulsed primary ion beam that hits the surface with an oblique trajectory and, for lipid analysis, the source of the beam most commonly consists of a cluster of ions as opposed to atomic primary ions, as this increases the detection of intact secondary molecular ions (Kraft and Klitzing, 2014). Similarly to MALDI, application of matrix has been also employed to increase the ionization of the sample however, given the high resolution of SIMS, the redistribution of the molecules on the surface of the sample due to the solvent in the matrix is an important limiting consideration. Because of this complication, the application of a thin layer of metal is perhaps most suitable for this method (Altelaar et al., 2006). Additionally, the application of complex statistical methods like multivariate analysis, have helped in the assignment and sorting of the spectra. In particular, PCA has been utilized to interpret the complex and often times nonspecific spectrum profiles obtained with TOF-SIMS (Graham and Castner, 2012) while partial least squares regression (PLSR) models have been used for quantification of the analytes but only in well-defined model systems (like model membranes) where calibration samples can be set up (Wilson and Kraft, 2013). Given the level of resolution of TOF-SIMS, the method is also able to image lipids at the single cell level, although currently it is only possible to detect the most abundant lipid classes and at a lateral resolution above 1um (Kraft and Klitzing, 2014).

NanoSIMS allows the detection of the monoatomic or diatomic secondary ions compared to the molecular ions and larger fragment ions analyzed by conventional SIMS. As these smaller ions are relatively abundant when using SIMS, the possibility of detecting and integrating them to generate specific spectra has a definite advantage. Moreover NanoSIMS is also more efficient in generating secondary ions from the samples then traditional SIMS. Importantly, these characteristics allow an astonishing planar resolution of approximately 50–100 nm for the imaging of lipids (Williams, 2006; Frisz et al., 2013a). In case of lipid analysis, it is also possible to label the sample with specific stable isotopes in order to visualize each class of lipids as a whole (i.e. using the (Wu et al., 2010) N isotope for labeling SPLs). This approach was used to perform studies at the single cell levels and to visualize the plasma membrane and subcellular structures while also reconstructing 3D views (Frisz et al., 2013a; Yeager et al., 2016). In this case, cells are grown directly onto conductive or semiconductive supports and are labeled isotopically to specifically trace the lipids of interest. Through the appropriate tuning of the primary ion dose, conditions are set such that the sputtering depth does not exceed the thickness of the membranes (approx. 7.5 nm) and/or to erode progressively the surface of the sample to acquire increasingly deeper views (Kraft and Klitzing, 2014).

4. Ambient ionization MS

4.1. Desorption electrospray ionization (DESI)

As compared to MALDI and SIMSs, DESI offers the advantage of little or no sample preparation, it is conducted at atmospheric pressure under ambient conditions and the analytes are directly desorbed/ionized from the sample surface allowing real-time MS measurements (Fig. 1). On the other hand, this method in its traditional setting provides poorer spatial resolution than MALDI. The first lipid imaging analysis with this method was reported in 2005 (Wiseman et al., 2005). In this method, the biological sample is sprayed with charged droplets of solvent carried by a nebulizing gas (Fig. 1). When these primary droplets hit the sample, the lipids are desorbed in the solvent and, as other primary droplets continue to strike the sample, secondary droplets containing the extracted lipids are splashed in the air. The airborne secondary droplets are ionized by an ESI-type of mechanism and delivered to a mass spectrometer through a heated extended capillary. Appealing positive features of this particular method include the fact that the fresh frozen tissue sample is generally mounted on glass without the need of a complex preparation (no matrix is needed) and that the analysis occurs at atmospheric conditions, greatly facilitating the practical operations. Also most lipids are detected as intact ions with minimal fragmentation (“soft ionization”) favoring the specificity of the analysis and also the detection of small lipid molecules. However, the lateral resolution of the spectra generated with this method is typically in the hundreds of microns, which is significantly less than that obtained with other MSI methods like MALDI, however resolution as low as 40um has also been achieved (Campbell et al., 2012). The solvents used are generally a mixture of water with methanol or acetonitrile, but other mixtures can also be employed with or without the addition of acidic modifiers depending on the class of lipid of interest. The use of these solvent mixtures causes extensive damage during the analysis preventing the use of the same slide for complementary analysis. However, it has been shown that a mix of dimethylformamide with ethanol or acetonitrile would allow the analysis of certain classes of phospholipids and sulfatides by DESI in negative ion mode followed by MALDI and histology Eberlin et al. (2011). Although detection of SPLs was not reported, the preservation of the sample and its further utilization for pathologic evaluation represented a significant development as DESI could be integrated in routine clinical tissue analysis work flow leading to the intraoperative use of this technique (Pirro et al., 2017).

Improved spatial resolution could be obtained by nanoDESI where the primary stream of micro-droplets is replaced by two micrometer-size fused silica capillary tubes, one of which is continuously infused by highly charged solvents and the second is used to aspirate the analytes from a tiny liquid junction formed on the targeted tissue surface. Typically, nanoDESI achieves spatial resolution around 100–150 um. Of note, a modification of this system into a single capillary probe has recently allowed to analyze individual Hela cells in situ (Pan et al., 2014) and to produce lipid images in mouse kidney section with an impressive spatial resolution of approximately 8.5um (Rao et al., 2015).

5. Applications

5.1. MSI for SPLs in tissues

5.1.1. Neurophysiology and brain injury

MSI has been applied to define the specific local distribution of SPLs or lipids in general both in normal neuronal tissues and in diseased situations.

For instance, using DESI-MSI, a 3D model of the mouse brain was constructed based on the distribution of PS(40:6), particularly enriched in the gray matter and of sulfatides(24:1), enriched in the white matter. The addition of spectral information of other lipids added more detailed anatomical features highlighting the specificity of the lipid distribution in this organ; in this study, however no analysis of SPL levels/distribution was reported (Eberlin et al., 2010a). To gain more complete lipid coverage, the use of polyvinylpyrrolidone capped silver nanoparticles was recently reported as matrix for MALDI imaging which increases the ionization of more difficult lipid molecules like free fatty acids or cholesterol (Guan et al., 2018). In this case, 10 classes of lipids were simultaneously analyzed in the mouse brain, with distinct localization of specific SM species (i.e. SM d18:1/18:0 localized in the cortex, hippocampus and cerebellum while SM d18:1/20:0 and 22:0 primarily localized in the thalamus).

Another study linked the distribution of specific molecular species of SM in the brain with the *in situ* expression of specific ceramide synthases (CerSs) (Sugimoto et al., 2015). In fact, the distinct substrate preference of this class of enzymes leads to production, by each CerS isoform, of distinct ceramide species which are thought to dictate tissue specific profiles of more downstream complex SPLs, like SMs (Levy and Futerman, 2010). Lipid images were acquired using FTICR-MALDI at a spatial resolution of approximately 100um and they showed preferential localization of SMd18:1/18:0 in the gray matter (rich in cell bodies) and SMd18:1/24:0 and 24:1 in the white matter (rich in myelin). Detection of CerSs expression by *in situ* hybridization aligned the distribution of SMs with the distinct localization of CerS1 (which produces (dh)CerC18) and of CerS2 (which produces (dh)CerC22 and C24) (Levy and Futerman, 2010). Importantly, this was one of the first approaches to go beyond the simple recording of SPL distribution in a given tissue by providing a more functional link to the enzymes that contribute to the regulation of the lipid levels.

In complementary studies, DESI imaging of cross sections of rat spinal cord at 200um resolution showed that glycerolipids and SM (42:1) were mostly detected in the white matter while FFA were present in the gray matter; however the analysis in positive ion mode for PC and SM delivered a low signal to noise ratio that greatly diminished the quality of the images compared to the enhanced detection of other PLs and FFA in the negative mode (Girod et al., 2010). A more in depth analysis of the normal structure and molecular lipid composition of mature rat sciatic nerve was achieved by MALDI (Fernandez et al., 2016). Both positive and negative ion mode MALDI was applied together with LC–MS/MS to obtain a more complete, precise and quantitative identification of the lipid species. Three anatomical regions were identified by their distinct lipid composition: the nerve fibers, rich in PCs, Hexosylceramides, SMs, PAs (positive mode) and sulfatides and PIs (negative mode); the connective tissue, generally enriched in complex SPLs (positive mode); and the adipose tissue surrounding the nerve, rich in TGs, DAGs, lactosylceramide (positive mode), PEs and PIs (negative mode). Of note, different C1P species and ceramide phosphoethanolamine (CPE) were also detected in this tissue, with C1P (d44:2) highly enriched in the connective tissue, other C1P species largely represented in the adipose tissue, and CPE present in both the fibers and adipose tissue.

Most recently, the lipid signature of the subventricular zone (SVZ), the largest area of plasticity in the adult human brain, was also analyzed by MALDI-MSI to gain information on the presence and distribution of specific lipids because of their emerging roles in neural stem cell biology (Hunter et al., 2018a). Indeed coordination of lipid synthesis and metabolism is involved in regulating the transition of neural stem cells from a quiescent (non-proliferating) to an active (proliferating) state, which in part occurs in the SVZ of the lateral ventricles (Codega et al., 2014; Shin et al., 2015; Hamilton et al., 2015). The results showed a specialized distribution of lipids within the human SVZ in the four anatomically distinct layers: enrichment of PIs in the superficial ependymal layer (lamina I) that interfaces with the ventricular cavity and contains ependymal cell bodies and astrocytic processes; enrichment in SMs in the hypocellular layer (lamina II) that contains few cell bodies but houses a dense network of astrocytic processes; no discrete lipid signature in the astrocytic ribbon with resident neural stem cells (lamina III); and finally enrichment in TGs and sulfatides in the heavily myelinated zone (lamina IV) that transitions to the underlying parenchyma of the caudate nucleus (CN). Thus it seems that the most abundant lipid classes in each layer align closely with the specific function of that layer. Interestingly, a change of the lipidome in the SVZ was observed postmortem in subjects with Huntington's disease, a neurodegenerative disease where thickening of the niche and enhanced proliferation has been observed (Hunter et al., 2018b). In this pathological condition, loss of sulfatides and TGs was observed in the myelin layer of the SVZ with an ectopic and focal accumulation of SMs and C1P; also, PIs were greatly reduced in the ependymal layer.

MALDI-TOF analysis was first applied to two rat brain injury models: ischemia/reperfusion after bilateral occlusion of the carotid artery and traumatic brain injury (TBI) (Hankin et al., 2011). In the first model, the phospholipid profile was altered especially in the cornu ammonis 1 region along with a significant accumulation of ceramide (d18:1/18:0) identified as the ion at m/z 548.5. Also localized accumulation of ceramide was observed in TBI. On the other hand, no measurements of SM were reported for either model in this study. Similar changes in ceramide were reported in a separate study of ischemia using MALDI-MSI after *in situ* desalting; this step removed the large fluctuations in cations that occur as consequence of the damage, greatly simplifying the interpretation of the spectra of the lipids in the brain tissue (Wang et al., 2012). This study showed the large remodeling of PC species after injury and confirmed the previously noted increase in ceramide (d18:1/18:0). Furthermore, the ceramide changes paralleled a concomitant decrease of SM (d18:1/18:0) in areas of the brain where SM levels are generally moderate to high. A recent study employing a murine model of permanent focal cerebral ischemia and the use of DESI and MALDI-MSI evaluated the lipid changes over time and found that the accumulation of ceramide (d18:1/18:0) and disappearance of SM (d18:1/18:0) at the site of ischemia occurred between 2 and 24 h from the insult (Fig. 2) (Nielsen et al., 2016). Interestingly, the study also revealed the appearance of C1P (d18:1/16:0) and sphingosine-1-phosphate (S1P) at day 7 during the resolution phase (Fig. 3) (Nielsen et al., 2016).

Changes in ceramide and SM were also observed in rat and mouse models of mild TBI (Roux et al., 2016; Woods et al., 2013). In particular, MALDI-TOF with a matrix of silver nanoparticles deposited over unfixed cryostat brain sections, showed that, in rats, the kinetics of the lipid changes might be different depending on the lipid molecules, with ceramide accumulating as early as 1 day post injury and other lipid changes occurring between 3 and 7 days post injury (Roux et al., 2016). Most interestingly, additional results from the same laboratory showed that ceramide levels were significantly reduced upon treatment of TBI with a peptide agonist (Barbacci et al., 2017), suggesting that ceramide changes could potentially represent a biomarker for brain injuries and for the response to treatment.

Also, MALDI-MSI with 1,5-diaminonaphthalene matrix deposition by sublimation and 10um lateral resolution revealed the local accumulation of ceramide and gangliosides to cortical and hippocampal ß-amyloid plaques visualized in brain tissue from transgenic Alzheimer's mice (tgArcSwe). The accumulation of ceramides and gangliosides was observed in the vicinity of the plaque regions where sulfatides were

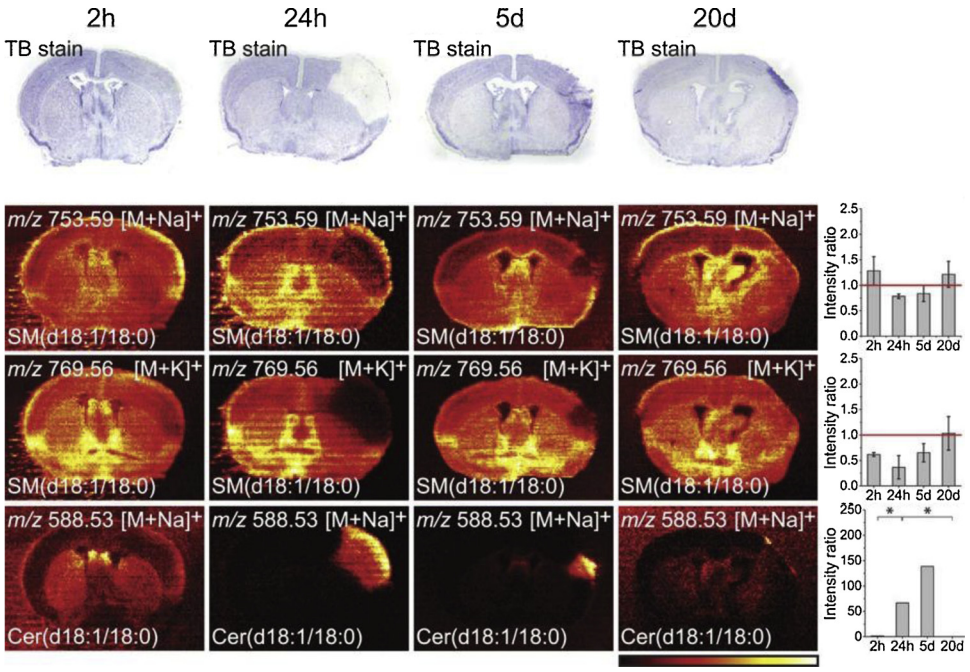

Fig. 2. MSI brain images of SM and Ceramide by DESI in a murine model of cerebral ischemia. Mouse brains at 2 h, 24 h, 5 days and 20 days after permanent middle cerebral artery occlusion were analyzed. Upper panels are images of brains stained with Toluidine Blue (TB) captured on Stemi DV4 stereoscope. The ion images have individual intensity bars between 0–100%, and therefore, the intensity colors cannot be compared between two images. For each lipid, the ratio between the intensity of the ischemic area and the comparable size area in the contralateral site are shown on the right side where bars are mean ± SEM (n = 3), *p < 0.05. The red line indicates ratio = one. Both the sodium and potassium adducts of SM(d18:1/18:0) disappeared from the area probably caused by sphingomyelinase degrading SM to Cer. Cer (d18:1/18:0) accumulated in the ischemic area at 24 h and 5d. All images were measured in positive ion mode by DESI imaging with a spatial resolution of 100 × 100 μm^2 and the images are a typical representative of 3 mice. This figure is adapted from Nielsen et al (Nielsen et al., 2016).

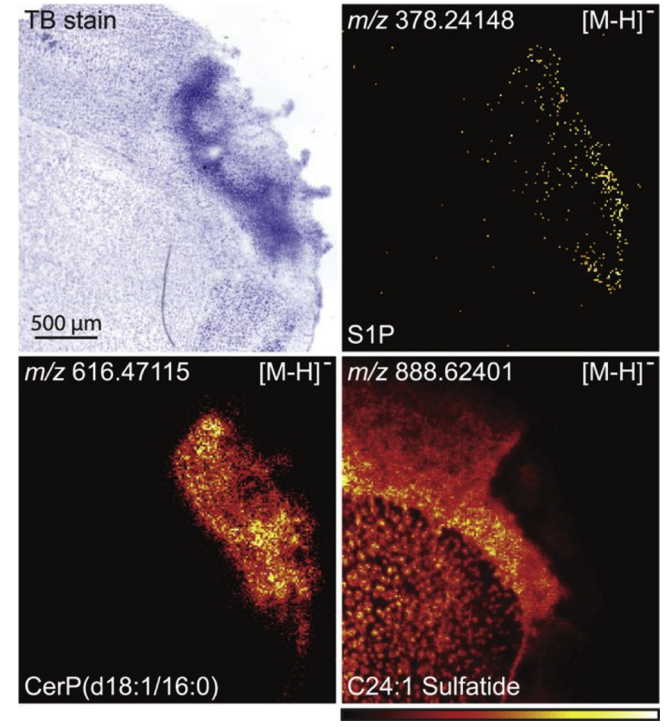

Fig. 3. MSI brain images of S1P, C1P and sulfitide by MALDI in a murine model of cerebral ischemia. Mouse brains at 7 days after permanent middle cerebral artery occlusion were analyzed. TB panel shows image of brain stained with Toluidine Blue captured on Stemi DV4 stereoscope. S1P and C1P(d18:1/16:0) were found to accumulate in the ischemic area at 7d post-surgical survival. In contrast, C24:1 Sulfatide disappeared from the area. All images were measured in negative ion mode using MALDI imaging with a resolution of 15 × 15 μm^2 and the images are a typical representative of 3 mice. This figure is adapted from Nielsen et al (Nielsen et al., 2016).

decreased suggesting that possibly the altered metabolism of sulfatides contributed to the accumulation of toxic SPLs (Kaya et al., 2017b). In a follow up study using the same mouse model, a three-step multimodal MALDI-MSI was developed to allow first the analysis of lipids in both positive and negative mode and then, after recoating the same tissue slide with 2,5-dihydroxy-acetophenone, the detection and visualization of proteins (Kaya et al., 2017a). Thus images containing the simultaneous localization of ß-amyloid plaque-associated lipids and Aß peptide isoforms were acquired in the same tissue slice. This is a remarkable achievement considering the spatial resolution obtained (10um) and the fact that the exact same pixels on the tissue could be reanalyzed.

Changes in the SPL profile of the brain were also investigated with MALDI-MSI in two mouse models of sphingolipidosis: Farber Disease and Tay-Sachs and Sandhoff disease. Farber Disease (FD) was recapitulated in a mouse model by a homozygous inactivating mutation of the acid ceramidase gene (Asah1$^{P361R/P361R}$ mice) (Sikora et al., 2017). In the brain of these mice, LC–MS measurements revealed a general increase of many SPLs, such as Cer, hydroxy-ceramides, dihydroceramides, sphingosine, dihexosylceramides, and monosialodihexosylganglioside while monohexosylceramide and SM did not change by mass but their representation among brain SPLs decreased. Localization studies with MALDI-MS showed accumulation of both Cer (d18:1/16:0) and Cer (d18:1/18:0) in the FD brains and most interestingly, revealed specific distribution of these ceramides. Cer (d18:1/16:0) was detected at low levels in brain of wild type mice and it showed a greatly enhanced signal in FD brains with its localization primarily in the cerebellar granule cells layer, cerebral cortex, and paraventricular and medial thalamic nuclei while strikingly absent in cerebellar white matter. In contrast, Cer (d18:1/18:0) was mainly increased in septal nuclei and corpus callosum of FD brain. As the cerebellum plays a role in controlling motor coordination, the accumulation of Cer (d18/C16:0) and Cer (d18:1/18:0) in that region may be contributing to the motor deficits seen in the behavioral tests of FD animals. Because the FD model will be used for the testing of new genetic therapeutic approaches, the ability to monitor the sites of ceramide accumulation after therapeutic intervention will provide crucial tissue-specific outcome measures (Sikora et al., 2017). The Tay-Sachs and Sandhoff disease was recapitulated by the homozygous disruption of the *HEXB* gene and compared to the functionally normal heterozygote mice (Chen et al., 2008). MALDI imaging allowed for the first time to determine the colocalization of accumulated GM2 and asialo-GM2 glycosphingolipids specifically in the granular cell region of the cerebellum. On the other hand no substantial differences were noted in Tay-Sachs mice for levels and distribution of sulfatides which were found in

the myelinated fiber (white matter) region of the cerebellum and the brain stem.

Finally, it is well documented that high doses of alcohol are associated with neurotoxic effects possibly triggered by inflammation (Peters et al., 2008; Ward et al., 2009; Ehrlich et al., 2012; He and Crews, 2008); as specific SPLs are proinflammatory effectors, the impact of chronic consumption of alcohol on the levels and distribution of SM and ceramide in murine and human brains was studied using MILDI (matrix implanted laser desorption/ionization) MSI and MALDI-TOF (Roux et al., 2015; de la Monte et al., 2018). In both adults and young mice, significant changes were observed in ceramide and/or SM after chronic consumption of ethanol (Roux et al., 2015). The changes were complex as different patterns depending on the time of analysis, the cross section of the brain analyzed and the age of the animals were observed. However changes of few metabolically connected ceramide and SM molecular species were functionally correlated in the white matter across all groups. The localization of these associations might be relevant as white matter degeneration and demyelination is associated with alcohol abuse. Another evidence of lipid changes in the white matter of subjects with disorders from alcohol use was provided by MALDI-TOF analysis in negative ion mode of postmortem specimens of the frontal lobe white matter (de la Monte et al., 2018). In this case, the tissue samples were embedded in carboxymethyl-cellulose, cryosectioned, thaw mounted on indium tin oxide (ITO) coated glass slides and sublimed with DHB matrix. Using this method, it was found that alcohol consumption broadly decreased SPLs (in particular sulfatides and ceramide) and phospholipid levels however, similar to the murine studies, regional variations were apparent. Of note, the tissue samples employed in the study were formalin fixed.

Importantly, another study comparing fresh and formalin fixed brain tissue samples with MALDI found that, beside the fact that the buffers used for fixation promoted the formation of Na + adduct ions instead of K + adduct ions normally predominant in fresh tissues, the lipid images corresponded well between the two methods (Carter et al., 2011), opening up the possibility to utilize formalin-fixed samples for retrospective studies.

5.1.2. Kidneys

Many studies have reported the distribution of SPLs, and in particular of SMs, in kidneys as this organ presents high concentrations of this SPL compared to other organs like brain; however the specific function for the high SM levels in this tissue is not clear.

Interestingly, a specific spatial profile was revealed in rat kidneys using high resolution MALDI (with silver nanoparticles and a spatial resolution of 50um) whereby SM (d18:1/16:1) and SM (d18:1/24:0) were visualized in the cortex while SM (d18:1/18:0) was concentrated in the medulla region and within dot-like structures across the cortex, which are likely renal corpuscles of the nephron (Muller et al., 2015). The use of silver nanoparticles allows detection of intact ceramides, which is a major advantage over traditional organic matrices in which ceramides are usually detected as a fragment ion corresponding to a neutral loss of water and, similarly to SM, this study reported that also ceramides showed distinct and varying distribution depending on the fatty acid chain attached to the sphingosine backbone. Indeed a high Cer (d18:1/22:0) signal localized in the medulla region of the kidney, Cer (d18:1/24:0) and (d18:1/24:1) were found in the cortex across the cortical labyrinth and possibly in the renal corpuscles and adjacent tubules of the nephron, and Cer (d18:1/26:0) was detected only in the collecting tubules of the renal pelvis. In another study comparing kidneys from sphingomyelin synthase 2 (SMS2) knock out mice with wild type by quantitative FTICR-MALDI, the previous distribution of specific SM species was generally confirmed while also detecting SM (d18:1/22:0) in the medulla, SM (d18:1/16:0) at the border of the cortex with the medulla and SM (d18:1/24:1) mostly in the cortex (Sugimoto et al., 2016). Moreover, it was observed that loss of SMS2 caused little changes in SM levels, mainly minimally reducing the levels of SM (d18:1/24:0) and inducing moderate increases in the corresponding ceramide specie.

MSI of kidneys using FTICR-MALDI was also utilized to describe a clever experimental approach to assist the operator in the assignment of the isolated SPL molecular ions (Jones et al., 2014). This method took advantage of on-tissue digestion with exogenously added recombinant ceramidase or sphingomyelinase to enhance and confirm the specificity of the signals attributed to ceramide and SM and that of other metabolically linked SPLs. Also, the previously mentioned Asah1$^{P361R/P361R}$ mice (deficient in acid ceramidase activity and *in vivo* model for FD) were employed to validate the method as they are characterized by accumulation of ceramides (and many other SPLs like glucosylceramide) in various tissues and thus greatly facilitating the visualization of these lipids (Alayoubi et al., 2013). By using the Asah1$^{P361R/P361R}$ mice, in addition to validate the lipid assignments, the authors added to previous investigations on ceramide distribution within the kidney, by showing C18:0 ceramide mainly localized in the medulla, C16:0 and C24:1 ceramides in the cortex and the overall accumulation of the C24:1 SM evenly distributed throughout the kidney section. Moreover using Asah1$^{P361R/P361R}$ mice the authors also reported the detection and localization of S1P and C1Ps in the medulla and of different species of glucosylceramide in the cortex and/or medulla.

The levels and distribution of SMs in the kidneys have also been assessed in response to high fat diet in mice and in diabetic subjects and while one study saw no major differences (Sugimoto et al., 2016), another (using MALDI at 25um lateral resolution) identified SM (d18:1/16:0) as the molecular specie accumulated in the glomeruli (localized in the renal cortex) in the diseased conditions (Miyamoto et al., 2016). Of note, the ATP/AMP ratio was also elevated which is a change believed to cause the suppression of AMP-activated protein kinase in diabetes. Cell culture experiments showed also that treatment of mesangial cells with SM (d18:1/16:0) caused an increase of ATP through activation of glycolysis and possibly implicating SM synthase in such effect.

Finally, a report studying the toxic effects of bisphenol S to the kidney in mice identified accumulation of sphingosine (d18:0), ceramide (d18:2/24:1) and SM (d22:0/20:4) in this organ and, by using MALDI imaging, it differentially localized these increases to the pelvis, medulla and renal cortex, respectively (Zhao et al., 2018). While these species of ceramide and SM are not common, they have been also detected by ESI-MS in human fibroblasts (Valsecchi et al., 2007) and in human plasma (http://mrc2.umich.edu/sites/default/files/Lipidomics%20-%20Assay%20Description.pdf).

5.1.3. Heart and vasculature

The first images of SPLs (and other lipids) in the heart were obtained from rats with MALDI using implanted silver nanoparticles covering the whole organ and positive and negative ion modes (Jackson et al., 2014). Very diverse patterns could be observed for triacylglycerols (TGs), SMs, PE and PCs in positive ion mode. While SMs were concentrated in the outer edges of the heart sections, PEs were mostly concentrated in the center, TGs in the vessel area and PCs more evenly distributed throughout. In negative mode, more lipids were detected with PIs, PEs and cardiolipins (CLs) being the most abundant. In this case, different PIs molecular species showed different patterns of distribution localizing either at the vessel area or throughout the heart, and CLs localizing around the edges.

DESI and reactive DESI (when a reactant is included in the spray solvent) in positive ion mode were also applied to study the lipid composition and distribution of glycerophospholipids, SM, lysoPC and cholesteryl esters in human atherosclerotic plaque tissue (Manicke et al., 2009). Interestingly, different specific lipid profiles were identified within areas of the lipid-rich plaques: the areas of the plaque with the lowest amount of lipids was characterized by high relative levels of SM(16:0) and areas where the lipid concentration was high were characterized by one of two lipid profiles: a lipid profile similar to the one with low lipids (hence predominance of SM) or one with very high

PCs amounts compared to SM. Similarly, the distribution of cholesterol esters was detected more abundantly in certain lipid rich region of the plaque.

5.1.4. Lens

The spatial distribution of SPLs in porcine crystalline lens was studied using FTICR-MALDI with a 150um lateral resolution (Vidova et al., 2010). The cryosections of the lens were thaw-mounted on ITO glass slides by soft-landing onto a layer of ethanol to preserve the integrity of the tissue. The localization of seven SM species (all d18:1) and two C1Ps were obtained, and found that most SMs (particularly enriched in human lens) and C1Ps were more abundant in the nucleus (where older fiber cells reside) than in the cortex of the lens with the exception of SM 22:0 which exhibited the same abundance in both areas. Most interestingly, changes in the distribution of SMs were observed with age progression (Deeley et al., 2010). As lens age, they form an annular barrier between the nucleus and the cortex that impedes the diffusion of small molecules within the lens and that is thought to be linked to the development of age-related nuclear cataract. Remarkably, a distinct annular distribution of dihydroSM (d18:0/16:0) was observed in the barrier area in lens from older human subjects together with a clear increase of dhCer (d18:0/16:0) in the nucleus of the lens and possibly with changes in the spatial distribution of lysoSMs (Deeley et al., 2010; Pol et al., 2015). Although it is not known whether the changes in dhSM and dhCer are connected, it is possible that the accumulation of dhCer leads to the annular accumulation of dhSM and that these changes may have important consequences on the physical properties of the fiber cell membranes contributing to the formation of the barrier. DESI-MSI measurements in human lens (Ellis et al., 2010) and FTICR-MALDI in bovine lens (Le et al., 2012) largely confirmed the distribution of SPLs within the lens obtained by MALDI, with dhSM in the outermost and annular barrier regions, dhC1P in the transition area from the inner to the outer portion of the lens and dhCer concentrated in the nucleus.

5.1.5. Cancer

The majority of studies using MSI in cancerous tissues aimed at investigating changes in levels and distribution of SPLs between the cancer and the normal tissue while others have focused on different areas within the tumor itself. Several different types of tumors have been analyzed with MSI.

In its first application to biological tissue imaging, DESI was applied to metastatic human liver adenocarcinoma and found higher levels of SM(16:0) in the tumor compared to the normal tissue (Wiseman et al., 2005). In this study, the results were presented as a graph of the lateral distribution across the specimen (with 1 mm increments for each measurement) and, interestingly they showed increasing levels of SM in the tumor as function of the distance from the normal tissue. However, the functional relevance of this specific distribution of SM in the specimen was not apparent.

MALDI-TOF was instead utilized to analyze formalin fixed specimens of papillary thyroid cancer in comparison to freshly frozen tissues and similarly found increased levels of SM(34:1 and 36:1) in the tumor, along with several species of PCs and Pas (Wojakowska et al., 2018). Similar to brain studies (Carter et al., 2011), these results are particularly useful as they confirm that formalin fixed tissues can be used for retrospective analysis. Another study however using FTICR-MALDI found SM(22:0) and SM(24:1) to be lower in malignant thyroid cancer versus normal adjacent tissue (NAT) or in benign tumor versus NAT, respectively (Guo et al., 2014). In either case, no specific observations related to the local distribution of SMs within the tissue were provided by these studies.

Also DESI-MSI, in both positive and negative modes, was applied to tissue sections of canine spontaneous invasive transitional cell carcinoma of the bladder (a model for human invasive bladder cancer) and the adjacent normal tissue. In these tissues, phospholipids like PC, PS and PI were highest in the tumor specimen while, differently from liver and thyroid cancers, SM (d18:1/16:0) levels were higher in the normal tissue (Dill et al., 2009b). However, no additional information about the distribution of these lipids within the tumor or the normal tissue was reported.

Similarly, using AP-MALDI-TOF, lower levels of SM (d18:1/16:0) were found in prostate cancers isolated from patients after radical prostatectomy compared to adjacent normal tissue (Goto et al., 2015), but the biological significance of this difference is not clear as the levels of SM did not correlate with preoperative levels of PSA, Gleason score, pathological stage or with clinical outcomes. However, using this enhanced resolution techniques, a lateral resolution of less than 10um was obtained allowing the precise discrimination between tumor foci embedded in the normal epithelium and stroma. SMs were also among those phospholipids whose levels were mostly different between non-small cell lung cancer and normal adjacent tissue (Marien et al., 2015). In fact, SM was lower in the tumor compared to the normal parenchima whereas PIs showed the opposite profile. Somewhat different results, were reported in the analysis of one specimen of squamous NSCLC lung tissue where SMs (d18:1/16:0) and (d18:0/20:0) [but not SM (d18:1/18:0)], ceramides (d18:1/12:0) and (d18:1/16:0) and hexosylceramides (d18:1/22:1) and (d18:1/24:1) were all elevated compared to the normal lung. Finally, FTICR-MALDI in the positive ion mode was used to analyze the intensities and distribution of various PCs and SMs in mycosis fungoides (MF), the most common type of cutaneous T cell lymphoma (Xu et al., 2017). In this case, while SM (d18:1/16:0) and different species of PC were decreased in the tumor tissue, their levels were elevated in the sera of the patients.

An interesting step toward reaching beyond the descriptive nature of MSI analysis was taken using xenografts of MDA-MB-231 breast cancer cells and linking lipid analysis with the hypoxic region within the tumor using MALDI (Chughtai et al., 2013). In this study, the expression of the tdTomato red fluorescent protein as a hypoxia-response element-driven reporter gene allowed the identification of hypoxic areas within the tumor masses, and found that SM (d18:1/16:0) and acylcarnitine were enriched in hypoxic regions whereas lysoPC(d16:0) and PC (d16:0/16:0) were concentrated in necrotic and normoxic regions, respectively. An imaging study using DESI identified ceramide (d34:1) as also specifically present in necrotic breast cancer (Tata et al., 2016), while another found this same SPL to be present in low levels in metastatic thyroid cancer in the lymph nodes and enriched in the normal lymph node tissue; another ceramide molecular specie, cer (37:1) showed the opposite profile (Zhang et al., 2017).

MSI has been also applied to uncover potential lipid biomarker signatures for tumor identification and classification. In this case, the ability to identify a large number of analytes is critical. For example, in ovarian cancer, DESI was used to identify a lipid biomarker signature which could effectively distinguish between high-grade serous carcinoma (highly aggressive) and serous borderline ovarian tumors (clinically indolent) (Sans et al., 2017). Among the lipids in the signature there were various FFAs, glycerophospholipids, cardiolipins and ceramides. Results obtained using DESI-MSI on a limited number of brain tumor samples seem to suggest that sulfatides and galactosylceramides may be used to differentiate between astrocytomas and glyoblastomas and among the different stages of astrocytomas, potentially pointing to the use of this method and the analysis of these lipids for the diagnosis of brain tumors (Eberlin et al., 2010b). Finally, a recent pilot study using FTICR-MALDI on archived frozen brain tumors has identified SPLs as discriminating classifiers to distinguish pineoblastoma from the histologically similar medulloblastoma (Clark et al., 2018).

5.1.6. Additional studies

A comprehensive analysis of the localization of the lipidome in the porcine adrenal gland was reported by using FTICR-MALDI both in positive and negative mode. Altogether, the study identified and visualized an astonishing 544 total lipids (228 lipids in the positive mode and 398 in the negative mode). Quercetin was utilized as matrix in both

positive and negative mode and its high efficiency of ionization allowed the identification of 102 SPLs. SMs and ceramides were detected in all five layers of porcine adrenal gland with SMs being mostly localized in the capsule and medulla. Many low abundance SPLs were also detected and they mainly enriched in the medulla (Wang et al., 2014).

MALDI imaging was also utilized in a number of additional studies investigating the localization of SPLs in different tissues and in related pathological conditions. For instance, the imaging of SM (d18:1/16:0) by MALDI-TOF at 100um lateral resolution was a marker for neutophil infiltrates in the lungs of mice infected with the fungus *Cryptococcus neoformans* (Qureshi et al., 2010); (Qureshi et al., 2011). A perfect superimposition between SM (d18:1/16:0) and the neutrophils could be observed. As the neutrophils accumulated where the fungus increasingly colonized the lung, so did the SM signal visualized and confirmed by MS/MS. To the contrary, the distribution of SM (d18:1/24:1) was completely different, concentrated in the lymph nodes and almost absent from the rest of the lung, thus suggesting cell specific distribution of different SM species, with phagocytes (at the site of *C. neoformans* colonization) rich in SM (d18:1/16:0) and lymphocytic cells rich in SM (d18:1/24:1).

Imaging by MALDI-TOF was also employed to study lipid changes in infected lungs from a mouse model of cystic fibrosis (CF) (Caretti et al., 2017). It is known that patients with CF are more susceptible to chronic inflammation of the airways and bacterial infections. Interestingly, in a murine model of CF, a slight increase of *de novo* generated ceramide in inflamed lungs was detected by whole tissue MS. As ceramide has been linked to promotion of inflammation, this study further established a potential cause-effect function of this lipid in this CF model. To investigate the nature of these changes, MALDI imaging was instrumental to pinpoint the compartmentalized formation of ceramide in the alveoli where it correlated with alveolar inflammation and bacterial infection. Interestingly, inhibition of ceramide formation with myriocin loaded in solid lipid nanocarriers and instilled in the trachea prevented the accumulation of ceramide and of the proinflammatory lipid, lyso-PC while favoring the increase of the anti-inflammatory PC potentially suggesting a link between these metabolic pathways.

MALDI imaging was also used to evaluate the effectiveness of lipid-targeting drugs by monitoring both the drug and the lipid(s) of interest in the targeted tissue. For instance, it was reported that the antitumor drug and ceramide analogue LCL124, once injected intraperitoneally in mice bearing xenografts of K562 leukemia cells, reached the tumors as visualized by MALDI-MSI. FITCR-MALDI analysis of the excised xenografts revealed that ceramides, SMs and glucosylceramides accumulated in the tumors of the animals treated with the drug confirming the alteration of SPL metabolism induced by LCL124 (Jones et al., 2015a). A similar approach was also used to monitor the efficacy of drugs targeting S1P metabolism (Jones et al., 2015b).

The diagnostic potential of ceramide measurements by AP ion-source chamber for MALDI combined with a quadrupole ion trap time-of-flight (QIT-TOF) mass spectrometer at 10um lateral resolution was evaluated in the case of Dorfman-Chanarin syndrome (DCS), a skin disorder characterized by barrier abnormalities (Goto-Inoue et al., 2012). The chosen imaging set up, by using soft ionization and concentrating the ions of interest, largely decreased ion suppression and allowed the clear detection of lower abundance lipids like acylceramides. Indeed loss of acylceramides and TGs accumulation was appreciated in the stratum corneum of the skin of patients with DCS and the imaging of the different skin strata revealed that the loss of acylceramides was likely due to reduced synthesis rather that a mislocalization of the lipid. Also, in the same study, the distribution of different species of SM, C1P and glucosylceramide through the mouse footpad was obtained.

Other reports have studied the distribution of SPLs in healthy placentas and in pathological conditions. For instance, SM has been specifically found in stem villi and PC in terminal villi of healthy placentas while their loss was reported in malperfused placentas (Yamazaki et al., 2015). Also, altered levels of placental ceramide were linked to preeclampsia localizing the ceramide increase to the trophoblast layers and syncytial knots of affected placentae (Melland-Smith et al., 2015). In this case, dysregulagion of acid ceramidase and *de novo* ceramide synthesis were proposed as the metabolic mechanism for the accumulation of ceramide and induction of autophagy in this model.

Finally, it has also been reported that SM (d18:1/16:0) is enriched in the stratified epithelium of mouse tongue with a distribution that corresponds to the nerve tissue relating to taste (Enomoto et al., 2011), and that accumulation of SM (d18:1/16:0), together with that of few other lipids, was observed at the site of varicose veins valve as compared to normal vein tissue (Tanaka et al., 2010). However, the implications of these findings are not known.

5.2. MSI for SPL studies in single cells

The analysis of single cells is a hot topic in MSI but it is yet to be perfected. In general, TOF-SIMS is the method that allows the highest resolution to image whole cells but it involves extensive fragmentation which reduces the confidence of the identification of the analytes. The analysis is generally limited to $m/z < 500$ but modifications such as matrix-enhanced SIM and metal-assisted SIMS have reduced fragmentation and extended the range of the m/z to approximately 1000 (Altelaar et al., 2006). Also a significant development of this technique is the ability to generate 3D images of the detected lipids through the cell. For instance, in the first report of this kind, cholesterol and other unspecified lipids (m/z at 255, at 540–570, and at 800–1000) were mapped as a function of depth in freeze-dried *Xenopus laevis* oocytes (Fletcher et al., 2007). These results were obtained using buckminsterfullerene (C60) as the primary ion source which has the ability to generate chemical images of surfaces with high sensitivities and minimal chemical damage. In a follow up report, TOF-SIMS was used to study the early stages of embryonal development of the *Xenopus laevis* with a subcellular lateral resolution of 4um (Tian et al., 2014). Interestingly, the dynamics of lipid remodeling during fertilization and early development were documented with the appearance on the surface of discrete small areas rich in PCs (towards the outer ring of the area), SMs (towards the inner circle), diacylglycerol and cholesterol (in the center) and potentially representing the points of fusion between the egg and the spermatozoa. As the fertilized egg divides, the lipid distribution becomes more evenly distributed throughout the surface with PC continuing to segregate from SM, cholesterol, monoacylglycerol and diacylglycerol.

MALDI-based techniques on the other hand, offer a wider m/z range of analysis and confidence in the identification of the parent compounds but the pixel resolution in its traditional applications can only reach approximately 50um, which does not allow resolution at the single cell level. However, a recent modification has achieved pixel resolution of approximately 7um and the assignment of accurate mass measurement with high resolution AP-MALDI (Rompp et al., 2010; Schober et al., 2012). In this study, Hela cells were directly grown on glass slides coated with ITO and fixed in 0.25% glutaraldehyde; DHB was then applied using a pneumatic sprayer and detection of various species of PC and SM were reported. MALDI imaging has also been applied to cultures of breast cancer cells for the identification of potential lipid signatures that would correlate with the different invasive phenotype of the cells (Wang et al., 2016). The 4 cell lines used were directly grown on ITO glass slides and coated with 9-aminoacridine as matrix. The study identified more than 450 endogenous compounds and among those, approximately 40 lipids correlated (positively or negatively) with the cells invasive activity and in particular, SM levels were low in the most invasive cell lines. These results were also in line with another study that applied FTICR-MALDI (He et al., 2015).

Possibly, the most recent development in this area is the analysis of mouse live hippocampal tissue slices under open-air atmospheric pressure and ambient temperature conditions at the subcellular level

(Kim et al., 2017). The method is based on an efficient desorption process by femtosecond laser assisted with nanoparticles (for enhanced desorption) and a subsequent ionization step by applying nonthermal plasma, termed AP nanoparticle and plasma assisted laser desorption ionization (AP-nanoPALDI) MS method. Combining the AP-nanoPALDI with microscopic sample scanning, a MS imaging with an astonishing spatial resolution of 2.9 μm was obtained. This level of resolution allowed subcellular analysis and revealed differences of molecular composition between the apical and basal dendrite regions of the hippocampal tissue. Interestingly, different SPLs were detected, with sphinganine and sphingosine enriched in the apical dendrite area and ceramide equally distributed between the two. Furthermore treatment of the hippocampal tissue slices with methyl β-cyclodextrin caused the loss of the ceramide signal and a dramatic rearrangement of both sphingosine and sphinganine patterns within the hippocampus.

5.3. MSI in plasma membrane and model membranes

The application of high resolution MSI techniques to the study of how lipids organize themselves in the membranes is particularly suitable since this technique has a level of resolution that can deliver precise information and, in model membranes, it is not significantly impacted by some of the complications that hinder the identification of the analytes in complex samples (such as large background peaks, low abundance and ion suppression). The application of these methods to the study of (sphingo)lipids in plasma membranes and model membranes has delivered a number of important and sometimes controversial observations. NanoSIMS allows visualization of discrete portions of the cell (at a 50 nm lateral resolution and 5 < nm depth of analysis of at the cell surface) and its application to intact cells has allowed the groundbreaking visualization of lipid microdomains in the plasma membrane (Frisz et al., 2013a). Indeed, after specific isotopic labeling of SPLs and other fatty acid carrying lipids, the existence of discrete SPL-rich microdomains was demonstrated in fibroblasts. It was revealed that SPLs organize in micrometer-wide areas composed of numerous microdomains of about 200 nm diameter. Partial removal of cholesterol led to the reorganization of these domains which appeared fewer and smaller. Importantly, this study found these SPL-rich microdomains to be functionally linked to cortical actin, as disruption of the cytoskeleton completely dismantled them, and disputed the concept of floating SPL-rich lipid rafts. Even more controversial was the subsequent finding that cholesterol did not enrich in such SPL-rich microdomains (Frisz et al., 2013b) against widely believed hypothesis. (Simons and Ikonen, 1997; Lingwood and Simons, 2010) Subsequently, 3D images also obtained with NanoSIMS analysis were reconstructed to show cholesterol and SPLs distribution in discrete and apparently separate subcellular structures across a portion of Madin-Darby canine kidney cells (Yeager et al., 2016).

TOF-SIMS and NanoSIMS have been both employed in studies addressing SPL organization within model membranes. Using TOF-SIMS, the effect of the level of phospholipid unsaturation in the formation of SM and cholesterol rich microdomains was studied using ternary lipid mixtures composed of PC, SM and cholesterol. Most surprisingly, it was suggested that the favorable interaction between SM and cholesterol is due to the saturated fatty acyl chain characteristic of SM rather than to the formation of hydrogen bonds between the sphingoid backbone and the hydroxyl on cholesterol (Zheng et al., 2007). However, these domain structures were only observed when an unsaturated lipid was present in the mixture (either PC or SM); in fact, for ternary mixtures with PC and SM both saturated (or unsaturated) no distinct microdomains could be observed. These observations were also confirmed in NanoSIMS studies using a ternary mixture containing two saturated PC species and different concentrations of cholesterol (Anderton et al., 2011). In a different study, when the ganglioside GM1 was also added to the mix together with SM, unsaturated PC and cholesterol, microdomains were observed mostly composed of GM1 and cholesterol with the presence of tiny SM-rich subdomains; however the vast majority of SM was found outside the microdomains together with unsaturated PC (Lozano et al., 2013). Finally, the formation of large ceramide-enriched platforms has been recently reported on the plasma membrane in response to specific stress inducers, such as Fas-ligand or bacterial infections (Zhang et al., 2009). Therefore the effect of addition of ceramide to a ternary mixture composed of unsaturated PC, saturated SM, and cholesterol was also studied using a combination of TOF-SIMS and Atomic Force Microscopy, and in this case, it was observed that ceramide concentrated in subdomains within the SM-cholesterol microdomains (Popov et al., 2008).

5.4. Other applications of MSI for lipids

Coupling MALDI MSI with Thin Layer Chromatography (TLC). One additional reported application of MALDI imaging is the detection of lipid classes (mostly phospholipids) after separation on TLC. Indeed MALDI imaging analysis of a developed TLC plate revealed a number of phospholipid spots that were not visible after traditional staining techniques (Fuchs et al., 2008). Moreover, the application of MALDI to each spot allowed for more detailed information about the composition of each lipid spot. However, it is to be considered that a UV laser cannot penetrate deeply through the silica hence only lipids that are toward the surface of the TLC are detected; this poses limitations for the precise quantification of the results since different lipids in the same spot can be distributed differently through the depth of the silica. For this, MALDI instruments equipped with infrared lasers (IR-MALDI) are better suited for quantitation. (Fuchs et al., 2010) An alternative procedure calls for the transfer of the lipid spots from the TLC plate to a PVDF membrane by applying heat (Zaima et al., 2011). The PVDF membrane is then mounted and processed for MALDI MSI providing better sensitivity and resolution and less background noise compared to direct analysis of the TLC plate (Guittard et al., 1999). The separation of the lipids previous to MALDI analysis reduces ion suppression effects favoring detection of the less abundant lipids. The use of this technique as opposed to liquid chromatography coupled to MS is advantageous because it is simple, fast (many samples can be separated at the same time) and cost effective.

TLC separation has also been coupled with DESI for lipid analysis but without obtaining imaging data. In this set up, thin tissue slices from rat brain were directly mounted on the TLC plate and lipids were eluted, and gangliosides partially separated and directly analyzed from the plate in negative ion mode (Wiseman and Li, 2010).

MALDI imaging has also been used in *forensic analysis* to reconstruct latent fingerprints by detection of lipids such as cholesterol, DAG, and free fatty acids (oleic and stearic acid) (Wolstenholme et al., 2009). However the application of traditional matrices greatly damages the print that cannot be used for further analysis. Importantly, the application of silver clusters by soft-landing ion mobility improves this aspect, facilitating in particular the analysis of low mass molecules (like lipids) without damaging the print (Walton and Verbeck, 2014).

One of the most remarkable applications of MSI is in the operating room where MALDI- and DESI-MSI have been utilized to assist in the *assessment of intraoperative surgical margins during cancer resection* (Pirro et al., 2017; St John et al., 2016). The importance of this step is underscored by the fact that positive margins are directly linked to a higher rate of local recurrence. For analysis with DESI-MSI, the tissue specimens are collected from the operating table, flash-frozen, sectioned and analyzed by MS to look for validated specific tumor-associated chemical fingerprints that indicate the residual presence of cancer cells at the surgical margins. Based on the discussion in the previous sections highlighting differences in the lipidome between normal and tumor tissues, it is not surprising that specific lipid patterns have been utilized to analyze the surgical margins (Eberlin et al., 2013; Jarmusch et al., 2016a, b). In their most efficient intraoperative set ups (like the Rapiflex MALDI instrument by Bruker), MALDI and DESI-MSI

techniques add just a few minutes of processing time for each sample to the surgical procedure. Also other MS based approaches are being implemented in the operating room, such as rapid evaporative ionization MS (REIMS) or the use of sampling probes (Schafer et al., 2009). For example, REIMS allows the analysis of the tissue-derived gaseous ions ("smoke") from commonly used thermal ablation surgical methods (electrosurgery and infrared laser surgery) in real-time (Golf et al., 2015; Balog et al., 2013).

Thus, it is apparent from this discussion that the study of SPLs and lipid in general has significantly contributed to a large variety of applications and impressive progress is being made with the implementation of these imaging techniques.

6. Final considerations

As the importance of cell specific functions of SPLs is recognized and the existence of the subcellular compartmentalization of SPL-mediated signaling is becoming ever more apparent (Hannun and Obeid, 2018; Ogretmen, 2018; Pyne et al., 2018; Newton et al., 2015), there is the need to find experimental tools able to probe these different aspects. MSI could represent one of the answers to these challenging issues.

Currently, MSI applied to lipids is a young discipline that is showing some promise as a complementary approach to more traditional techniques, and as we move forward with its application to lipid research, important challenges include: 1. improving sensitivity (to more confidently and quantitatively detect low abundance SPLs); 2. increasing resolution (to gain information at the cellular and subcellular levels); and 3. providing functional meaning to the images of SPLs within tissues.

Progress in each of these aspects requires skills and creativity. For instance, the clever approach of applying in-situ-digestion for validation of lipid analytes adds confidence to their identification and exemplifies a way to gain more precise information (Jones et al., 2014). The sequential application to the same tissue section of TOF-SIMS and AP-MALDI allows to complement the high spatial resolution provided by the first with the confirmation of molecular structures by the second, bringing the analysis to cellular dimensions (Desbenoit et al., 2018). Also, novel MS strategies have been developed specifically to detect SPLs of particularly low abundance. One of these is the addition of a zinc complex that specifically binds to phosphate monoester residues (Phos-Tag) to MALDI-TOF for improved detection of S1P and C1P (Morishige et al., 2010; Yamashita et al., 2016). This approach was successfully applied to the analysis of several mouse tissues even allowing the identification of novel molecular species of C1P and, if applicable to MSI, could be particularly useful.

Furthermore, as mentioned previously, the Single-Probe modification of nanoDESI has been used to obtain single cell data from Hela cells *in situ* (Pan et al., 2014) and to produce MS images with high spatial resolution (8.5 μm) from biological samples such as mouse brain and kidney sections (Rao et al., 2015). While only PC measurements were reported in the latter study, it is anticipated that this technique will reveal very useful for high resolution MSI of SPLs in the future and could be instrumental especially in highly complex tissue samples.

As we are just starting to explore the potential of MSI techniques, so far most of the studies are of descriptive nature with some very intriguing observations, such as the differential distribution of SPLs across crystalline lens and their changes with age (Deeley et al., 2010; Pol et al., 2015). In the case of tissue imaging, the next step would be to provide some functional meaning to these images and this could be obtained for instance by associating metabolic relationships or specific biological events. Excellent examples of this next-level approach are for instance the correlation between the distribution of the different SM molecular species in the brain and the expression of the different CerSs (Sugimoto et al., 2015) or the colocalization of SMs with a reporter fluorescent protein for hypoxia in breast cancer xenografts (Chughtai et al., 2013).

It is also desirable that more dynamic studies are pursued to better understand SPL regulation and functions by evaluating the response to a specific "perturbation" (in case of *in vivo* studies, perturbations could be provided by testing different diets, the effect of metabolic inhibitors or loss of genes, or infections as a few studies have done) (Sikora et al., 2017; Chen et al., 2008; Sugimoto et al., 2016; Qureshi et al., 2010, 2011; Caretti et al., 2017). Progress in this direction can only be obtained by promoting access to MSI techniques, access that currently is available, for the most part, through collaborations, mostly for two reasons. First, given the nuances of the technique, the application of a "standard protocol" applicable by a Core Facility for a fee-for-service is probably still premature. Second, being MSI a cumbersome procedure in need of optimization on a case-to-case basis, it requires substantial time and dedication making studies through a Core Facility very costly. Adding to the challenges is the very limited number of laboratories that have the necessary expertise both in MALDI imaging and lipid chemistry.

However, similar challenges faced the quantitative analysis of SPLs by MS at the beginning and, in spite of that, it has now become the go-to method for SPL measurements; importantly, the application of MS methods has also contributed to establish new paradigms of SPL metabolism and signaling based on the uncovered molecular complexity of these molecules. So we foresee that MSI will have a similar revealing impact in its application to SPL research.

Conflict of interest

Dr. Maurizio Del Poeta is a Co-Founder and Chief Scientific Officer (CSO) of MicroRid Technologies Inc. The other authors have no conflict of interest.

Acknowledgements

The authors would like to thank Dr. Justin Snider and the lipidomics core facility at Stony Brook University for insightful discussions. This work was supported by NIH/NCI grant P01-CA097132 to CL for project #4, by NIH grants AI116420, AI125770, AI136934 to MDP, and by Merit Review grant I01BX002624 from the Veterans Affairs Program to MDP. Maurizio Del Poeta is Burroughs Welcome Investigator in Infectious Diseases.

References

Alayoubi, A.M., Wang, J.C., Au, B.C., Carpentier, S., Garcia, V., Dworski, S., El-Ghamrasni, S., Kirouac, K.N., Exertier, M.J., Xiong, Z.J., Prive, G.G., Simonaro, C.M., Casas, J., Fabrias, G., Schuchman, E.H., Turner, P.V., Hakem, R., Levade, T., Medin, J.A., 2013. Systemic ceramide accumulation leads to severe and varied pathological consequences. EMBO Mol. Med. 5, 827–842.

Alexandrov, T., 2012. MALDI imaging mass spectrometry: statistical data analysis and current computational challenges. BMC Bioinformatics 13 (Suppl. 16), S11.

Altelaar, A.F., Klinkert, I., Jalink, K., de Lange, R.P., Adan, R.A., Heeren, R.M., Piersma, S.R., 2006. Gold-enhanced biomolecular surface imaging of cells and tissue by SIMS and MALDI mass spectrometry. Anal. Chem. 78, 734–742.

Anderton, C.R., Lou, K., Weber, P.K., Hutcheon, I.D., Kraft, M.L., 2011. Correlated AFM and NanoSIMS imaging to probe cholesterol-induced changes in phase behavior and non-ideal mixing in ternary lipid membranes. Biochim. Biophys. Acta 1808, 307–315.

Balog, J., Sasi-Szabo, L., Kinross, J., Lewis, M.R., Muirhead, L.J., Veselkov, K., Mirnezami, R., Dezso, B., Damjanovich, L., Darzi, A., Nicholson, J.K., Takats, Z., 2013. Intraoperative tissue identification using rapid evaporative ionization mass spectrometry. Sci. Transl. Med. 5, 194ra193.

Barbacci, D.C., Roux, A., Muller, L., Jackson, S.N., Post, J., Baldwin, K., Hoffer, B., Balaban, C.D., Schultz, J.A., Gouty, S., Cox, B.M., Woods, A.S., 2017. Mass spectrometric imaging of ceramide biomarkers tracks therapeutic response in traumatic brain injury. ACS Chem. Neurosci. 8, 2266–2274.

Berry, K.A., Hankin, J.A., Barkley, R.M., Spraggins, J.M., Caprioli, R.M., Murphy, R.C., 2011. MALDI imaging of lipid biochemistry in tissues by mass spectrometry. Chem. Rev. 111, 6491–6512.

Campbell, D.I., Ferreira, C.R., Eberlin, L.S., Cooks, R.G., 2012. Improved spatial resolution in the imaging of biological tissue using desorption electrospray ionization. Anal. Bioanal. Chem. 404, 389–398.

Caretti, A., Vasso, M., Bonezzi, F.T., Gallina, A., Trinchera, M., Rossi, A., Adami, R., Casas, J., Falleni, M., Tosi, D., Bragonzi, A., Ghidoni, R., Gelfi, C., Signorelli, P., 2017.

Myriocin treatment of CF lung infection and inflammation: complex analyses for enigmatic lipids. Naunyn Schmiedebergs Arch. Pharmacol. 390, 775–790.
Carter, C.L., McLeod, C.W., Bunch, J., 2011. Imaging of phospholipids in formalin fixed rat brain sections by matrix assisted laser desorption/ionization mass spectrometry. J. Am. Soc. Mass Spectrom. 22, 1991–1998.
Chen, Y., Allegood, J., Liu, Y., Wang, E., Cachon-Gonzalez, B., Cox, T.M., Merrill Jr, A.H., Sullards, M.C., 2008. Imaging MALDI mass spectrometry using an oscillating capillary nebulizer matrix coating system and its application to analysis of lipids in brain from a mouse model of Tay-Sachs/Sandhoff disease. Anal. Chem. 80, 2780–2788.
Chughtai, K., Jiang, L., Greenwood, T.R., Glunde, K., Heeren, R.M., 2013. Mass spectrometry images acylcarnitines, phosphatidylcholines, and sphingomyelin in MDA-MB-231 breast tumor models. J. Lipid Res. 54, 333–344.
Clark, A.R., Calligaris, D., Regan, M.S., Pomeranz Krummel, D., Agar, J.N., Kallay, L., MacDonald, T., Schniederjan, M., Santagata, S., Pomeroy, S.L., Agar, N.Y.R., Sengupta, S., 2018. Rapid discrimination of pediatric brain tumors by mass spectrometry imaging. J. Neurooncol.
Codega, P., Silva-Vargas, V., Paul, A., Maldonado-Soto, A.R., Deleo, A.M., Pastrana, E., Doetsch, F., 2014. Prospective identification and purification of quiescent adult neural stem cells from their in vivo niche. Neuron 82, 545–559.
de la Monte, S.M., Kay, J., Yalcin, E.B., Kril, J.J., Sheedy, D., Sutherland, G.T., 2018. Imaging mass spectrometry of frontal white matter lipid changes in human alcoholics. Alcohol 67, 51–63.
Deeley, J.M., Hankin, J.A., Friedrich, M.G., Murphy, R.C., Truscott, R.J., Mitchell, T.W., Blanksby, S.J., 2010. Sphingolipid distribution changes with age in the human lens. J. Lipid Res. 51, 2753–2760.
Desbenoit, N., Walch, A., Spengler, B., Brunelle, A., Rompp, A., 2018. Correlative mass spectrometry imaging, applying time-of-flight secondary ion mass spectrometry and atmospheric pressure matrix-assisted laser desorption/ionization to a single tissue section. Rapid Commun. Mass Spectrom. 32, 159–166.
Dill, A.L., Ifa, D.R., Manicke, N.E., Ouyang, Z., Cooks, R.G., 2009a. Mass spectrometric imaging of lipids using desorption electrospray ionization. J. Chromatogr. B Analyt. Technol. Biomed. Life Sci. 877, 2883–2889.
Dill, A.L., Ifa, D.R., Manicke, N.E., Costa, A.B., Ramos-Vara, J.A., Knapp, D.W., Cooks, R.G., 2009b. Lipid profiles of canine invasive transitional cell carcinoma of the urinary bladder and adjacent normal tissue by desorption electrospray ionization imaging mass spectrometry. Anal. Chem. 81, 8758–8764.
Eberlin, L.S., Ifa, D.R., Wu, C., Cooks, R.G., 2010a. Three-dimensional vizualization of mouse brain by lipid analysis using ambient ionization mass spectrometry. Angew. Chem. Int. Ed. Engl. 49, 873–876.
Eberlin, L.S., Dill, A.L., Golby, A.J., Ligon, K.L., Wiseman, J.M., Cooks, R.G., Agar, N.Y., 2010b. Discrimination of human astrocytoma subtypes by lipid analysis using desorption electrospray ionization imaging mass spectrometry. Angew. Chem. Int. Ed. Engl. 49, 5953–5956.
Eberlin, L.S., Liu, X., Ferreira, C.R., Santagata, S., Agar, N.Y., Cooks, R.G., 2011. Desorption electrospray ionization then MALDI mass spectrometry imaging of lipid and protein distributions in single tissue sections. Anal. Chem. 83, 8366–8371.
Eberlin, L.S., Norton, I., Orringer, D., Dunn, I.F., Liu, X., Ide, J.L., Jarmusch, A.K., Ligon, K.L., Jolesz, F.A., Golby, A.J., Santagata, S., Agar, N.Y., Cooks, R.G., 2013. Ambient mass spectrometry for the intraoperative molecular diagnosis of human brain tumors. Proc. Natl. Acad. Sci. U. S. A. 110, 1611–1616.
Ehrlich, D., Pirchl, M., Humpel, C., 2012. Effects of long-term moderate ethanol and cholesterol on cognition, cholinergic neurons, inflammation, and vascular impairment in rats. Neuroscience 205, 154–166.
Eibisch, M., Schiller, J., 2011. Sphingomyelin is more sensitively detectable as a negative ion than phosphatidylcholine: a matrix-assisted laser desorption/ionization time-of-flight mass spectrometric study using 9-aminoacridine (9-AA) as matrix. Rapid Commun. Mass Spectrom. 25, 1100–1106.
Ellis, S.R., Wu, C., Deeley, J.M., Zhu, X., Truscott, R.J., in het Panhuis, M., Cooks, R.G., Mitchell, T.W., Blanksby, S.J., 2010. Imaging of human lens lipids by desorption electrospray ionization mass spectrometry. J. Am. Soc. Mass Spectrom. 21, 2095–2104.
Ellis, S.R., Brown, S.H., In Het Panhuis, M., Blanksby, S.J., Mitchell, T.W., 2013. Surface analysis of lipids by mass spectrometry: more than just imaging. Prog. Lipid Res. 52, 329–353.
Enomoto, H., Sugiura, Y., Setou, M., Zaima, N., 2011. Visualization of phosphatidylcholine, lysophosphatidylcholine and sphingomyelin in mouse tongue body by matrix-assisted laser desorption/ionization imaging mass spectrometry. Anal. Bioanal. Chem. 400, 1913–1921.
Farwanah, H., Kolter, T., Sandhoff, K., 2011. Mass spectrometric analysis of neutral sphingolipids: methods, applications, and limitations. Biochim. Biophys. Acta 1811, 854–860.
Fernandez, R., Carriel, V., Lage, S., Garate, J., Diez-Garcia, J., Ochoa, B., Castro, B., Alaminos, M., Fernandez, J.A., 2016. Deciphering the lipid architecture of the rat sciatic nerve using imaging mass spectrometry. ACS Chem. Neurosci. 7, 624–632.
Fisher, G.L., Bruinen, A.L., Ogrinc Potocnik, N., Hammond, J.S., Bryan, S.R., Larson, P.E., Heeren, R.M., 2016. A new method and mass spectrometer design for TOF-SIMS parallel imaging MS/MS. Anal. Chem. 88, 6433–6440.
Fletcher, J.S., Lockyer, N.P., Vaidyanathan, S., Vickerman, J.C., 2007. TOF-SIMS 3D biomolecular imaging of Xenopus laevis oocytes using buckminsterfullerene (C60) primary ions. Anal. Chem. 79, 2199–2206.
Frisz, J.F., Lou, K., Klitzing, H.A., Hanafin, W.P., Lizunov, V., Wilson, R.L., Carpenter, K.J., Kim, R., Hutcheon, I.D., Zimmerberg, J., Weber, P.K., Kraft, M.L., 2013a. Direct chemical evidence for sphingolipid domains in the plasma membranes of fibroblasts. Proc. Natl. Acad. Sci. U. S. A. 110, E613–622.
Frisz, J.F., Klitzing, H.A., Lou, K., Hutcheon, I.D., Weber, P.K., Zimmerberg, J., Kraft, M.L., 2013b. Sphingolipid domains in the plasma membranes of fibroblasts are not enriched with cholesterol. J. Biol. Chem. 288, 16855–16861.
Fuchs, B., Schiller, J., Suss, R., Zscharnack, M., Bader, A., Muller, P., Schurenberg, M., Becker, M., Suckau, D., 2008. Analysis of stem cell lipids by offline HPTLC-MALDI-TOF MS. Anal. Bioanal. Chem. 392, 849–860.
Fuchs, B., Suss, R., Schiller, J., 2010. An update of MALDI-TOF mass spectrometry in lipid research. Prog. Lipid Res. 49, 450–475.
Girod, M., Shi, Y., Cheng, J.X., Cooks, R.G., 2010. Desorption electrospray ionization imaging mass spectrometry of lipids in rat spinal cord. J. Am. Soc. Mass Spectrom. 21, 1177–1189.
Golf, O., Strittmatter, N., Karancsi, T., Pringle, S.D., Speller, A.V., Mroz, A., Kinross, J.M., Abbassi-Ghadi, N., Jones, E.A., Takats, Z., 2015. Rapid evaporative ionization mass spectrometry imaging platform for direct mapping from bulk tissue and bacterial growth media. Anal. Chem. 87, 2527–2534.
Goto, T., Terada, N., Inoue, T., Kobayashi, T., Nakayama, K., Okada, Y., Yoshikawa, T., Miyazaki, Y., Uegaki, M., Utsunomiya, N., Makino, Y., Sumiyoshi, S., Yamasaki, T., Kamba, T., Ogawa, O., 2015. Decreased expression of lysophosphatidylcholine (16:0/OH) in high resolution imaging mass spectrometry independently predicts biochemical recurrence after surgical treatment for prostate cancer. Prostate 75, 1821–1830.
Goto-Inoue, N., Hayasaka, T., Zaima, N., Nakajima, K., Holleran, W.M., Sano, S., Uchida, Y., Setou, M., 2012. Imaging mass spectrometry visualizes ceramides and the pathogenesis of dorfman-chanarin syndrome due to ceramide metabolic abnormality in the skin. PLoS One 7, e49519.
Graham, D.J., Castner, D.G., 2012. Multivariate analysis of ToF-SIMS data from multicomponent systems: the why, when, and how. Biointerphases 7, 49.
Guan, M., Zhang, Z., Li, S., Liu, J., Liu, L., Yang, H., Zhang, Y., Wang, T., Zhao, Z., 2018. Silver nanoparticles as matrix for MALDI FTICR MS profiling and imaging of diverse lipids in brain. Talanta 179, 624–631.
Guittard, J., Hronowski, X.L., Costello, C.E., 1999. Direct matrix-assisted laser desorption/ionization mass spectrometric analysis of glycosphingolipids on thin layer chromatographic plates and transfer membranes. Rapid Commun. Mass Spectrom. 13, 1838–1849.
Guo, S., Qiu, L., Wang, Y., Qin, X., Liu, H., He, M., Zhang, Y., Li, Z., Chen, X., 2014. Tissue imaging and serum lipidomic profiling for screening potential biomarkers of thyroid tumors by matrix-assisted laser desorption/ionization-Fourier transform ion cyclotron resonance mass spectrometry. Anal. Bioanal. Chem. 406, 4357–4370.
Hamilton, L.K., Dufresne, M., Joppe, S.E., Petryszyn, S., Aumont, A., Calon, F., Barnabe-Heider, F., Furtos, A., Parent, M., Chaurand, P., Fernandes, K.J., 2015. Aberrant lipid metabolism in the forebrain niche suppresses adult neural stem cell proliferation in an animal model of alzheimer's disease. Cell Stem Cell 17, 397–411.
Hankin, J.A., Murphy, R.C., 2010. Relationship between MALDI IMS intensity and measured quantity of selected phospholipids in rat brain sections. Anal. Chem. 82, 8476–8484.
Hankin, J.A., Farias, S.E., Barkley, R.M., Heidenreich, K., Frey, L.C., Hamazaki, K., Kim, H.Y., Murphy, R.C., 2011. MALDI mass spectrometric imaging of lipids in rat brain injury models. J. Am. Soc. Mass Spectrom. 22, 1014–1021.
Hannun, Y.A., Obeid, L.M., 2018. Sphingolipids and their metabolism in physiology and disease. Nat. Rev. Mol. Cell Biol. 19, 175–191.
He, J., Crews, F.T., 2008. Increased MCP-1 and microglia in various regions of the human alcoholic brain. Exp. Neurol. 210, 349–358.
He, M., Guo, S., Li, Z., 2015. In situ characterizing membrane lipid phenotype of breast cancer cells using mass spectrometry profiling. Sci. Rep. 5, 11298.
Hillenkamp, F., Karas, M., Beavis, R.C., Chait, B.T., 1991. Matrix-assisted laser desorption/ionization mass spectrometry of biopolymers. Anal. Chem. 63, 1193A–1203A.
Hunter, M., Demarais, N.J., Faull, R.L.M., Grey, A.C., Curtis, M.A., 2018a. Layer-specific lipid signatures in the human subventricular zone demonstrated by imaging mass spectrometry. Sci. Rep. 8, 2551.
Hunter, M., Demarais, N.J., Faull, R.L.M., Grey, A.C., Curtis, M.A., 2018b. Subventricular zone lipidomic architecture loss in Huntington's disease. J. Neurochem.
Jackson, S.N., Ugarov, M., Egan, T., Post, J.D., Langlais, D., Albert Schultz, J., Woods, A.S., 2007. MALDI-ion mobility-TOFMS imaging of lipids in rat brain tissue. J. Mass Spectrom. 42, 1093–1098.
Jackson, S.N., Baldwin, K., Muller, L., Womack, V.M., Schultz, J.A., Balaban, C., Woods, A.S., 2014. Imaging of lipids in rat heart by MALDI-MS with silver nanoparticles. Anal. Bioanal. Chem. 406, 1377–1386.
Jarmusch, A.K., Pirro, V., Baird, Z., Hattab, E.M., Cohen-Gadol, A.A., Cooks, R.G., 2016a. Lipid and metabolite profiles of human brain tumors by desorption electrospray ionization-MS. Proc. Natl. Acad. Sci. U. S. A. 113, 1486–1491.
Jarmusch, A.K., Alfaro, C.M., Pirro, V., Hattab, E.M., Cohen-Gadol, A.A., Cooks, R.G., 2016b. Differential lipid profiles of normal human brain matter and gliomas by positive and negative mode desorption electrospray ionization - mass spectrometry imaging. PLoS One 11, e0163180.
Jones, E.E., Dworski, S., Canals, D., Casas, J., Fabrias, G., Schoenling, D., Levade, T., Denlinger, C., Hannun, Y.A., Medin, J.A., Drake, R.R., 2014. On-tissue localization of ceramides and other sphingolipids by MALDI mass spectrometry imaging. Anal. Chem. 86, 8303–8311.
Jones, E.E., Dworski, S., Kamani, M., Canals, D., Wada, M., Liu, X., Hannun, Y.A., Norris, J., Medin, J.A., Drake, R.R., 2015a. Detection and distribution of sphingolipids in tissue by FTICR-MALDI-imaging mass spectrometry. Detection and Distribution of Sphingolipids in Tissue by FTICR-MALDI-Imaging Mass Spectrometry. in: Bioactive Sphingolipids in Cancer biology and Therapy. Springer International Publishing, Switzerland.
Jones, E.E., Gao, P., Smith, C.D., Norris, J.S., Drake, R.R., 2015b. Tissue biomarkers of drug efficacy: case studies using a MALDI-MSI workflow. Bioanalysis 7, 2611–2619.
Kaya, I., Brinet, D., Michno, W., Baskurt, M., Zetterberg, H., Blenow, K., Hanrieder, J., 2017a. Novel trimodal MALDI imaging mass spectrometry (IMS3) at 10 mum reveals

spatial lipid and peptide correlates implicated in abeta plaque pathology in alzheimer's disease. ACS Chem. Neurosci. 8, 2778–2790.
Kaya, I., Brinet, D., Michno, W., Syvanen, S., Sehlin, D., Zetterberg, H., Blennow, K., Hanrieder, J., 2017b. Delineating amyloid plaque associated neuronal sphingolipids in transgenic alzheimer's disease mice (tgArcSwe) using MALDI imaging mass spectrometry. ACS Chem. Neurosci. 8, 347–355.
Kim, J.Y., Seo, E.S., Kim, H., Park, J.W., Lim, D.K., Moon, D.W., 2017. Atmospheric pressure mass spectrometric imaging of live hippocampal tissue slices with subcellular spatial resolution. Nat. Commun. 8, 2113.
Korte, A.R., Lee, Y.J., 2013. Multiplex mass spectrometric imaging with polarity switching for concurrent acquisition of positive and negative ion images. J. Am. Soc. Mass Spectrom. 24, 949–955.
Kraft, M.L., Klitzing, H.A., 2014. Imaging lipids with secondary ion mass spectrometry. Biochim. Biophys. Acta 1841, 1108–1119.
Le, C.H., Han, J., Borchers, C.H., 2012. Dithranol as a MALDI matrix for tissue imaging of lipids by Fourier transform ion cyclotron resonance mass spectrometry. Anal. Chem. 84, 8391–8398.
Levy, M., Futerman, A.H., 2010. Mammalian ceramide synthases. IUBMB Life 62, 347–356.
Lingwood, D., Simons, K., 2010. Lipid rafts as a membrane-organizing principle. Science 327, 46–50.
Lohmann, C., Schachmann, E., Dandekar, T., Villmann, C., Becker, C.M., 2010. Developmental profiling by mass spectrometry of phosphocholine containing phospholipids in the rat nervous system reveals temporo-spatial gradients. J. Neurochem. 114, 1119–1134.
Lozano, M.M., Liu, Z., Sunnick, E., Janshoff, A., Kumar, K., Boxer, S.G., 2013. Colocalization of the ganglioside G(M1) and cholesterol detected by secondary ion mass spectrometry. J. Am. Chem. Soc. 135, 5620–5630.
Luxembourg, S.L., McDonnell, L.A., Duursma, M.C., Guo, X., Heeren, R.M., 2003. Effect of local matrix crystal variations in matrix-assisted ionization techniques for mass spectrometry. Anal. Chem. 75, 2333–2341.
Manicke, N.E., Nefliu, M., Wu, C., Woods, J.W., Reiser, V., Hendrickson, R.C., Cooks, R.G., 2009. Imaging of lipids in atheroma by desorption electrospray ionization mass spectrometry. Anal. Chem. 81, 8702–8707.
Marien, E., Meister, M., Muley, T., Fieuws, S., Bordel, S., Derua, R., Spraggins, J., Van de Plas, R., Dehairs, J., Wouters, J., Bagadi, M., Dienemann, H., Thomas, M., Schnabel, P.A., Caprioli, R.M., Waelkens, E., Swinnen, J.V., 2015. Non-small cell lung cancer is characterized by dramatic changes in phospholipid profiles. Int. J. Cancer 137, 1539–1548.
Melland-Smith, M., Ermini, L., Chauvin, S., Craig-Barnes, H., Tagliaferro, A., Todros, T., Post, M., Caniggia, I., 2015. Disruption of sphingolipid metabolism augments ceramide-induced autophagy in preeclampsia. Autophagy 11, 653–669.
Miyamoto, S., Hsu, C.C., Hamm, G., Darshi, M., Diamond-Stanic, M., Decleves, A.E., Slater, L., Pennathur, S., Stauber, J., Dorrestein, P.C., Sharma, K., 2016. Mass spectrometry imaging reveals elevated glomerular ATP/AMP in Diabetes/obesity and identifies sphingomyelin as a possible mediator. EBioMedicine 7, 121–134.
Morishige, J., Urikura, M., Takagi, H., Hirano, K., Koike, T., Tanaka, T., Satouchi, K., 2010. A clean-up technology for the simultaneous determination of lysophosphatidic acid and sphingosine-1-phosphate by matrix-assisted laser desorption/ionization time-of-flight mass spectrometry using a phosphate-capture molecule, Phos-tag. Rapid Commun. Mass Spectrom. 24, 1075–1084.
Muller, L., Kailas, A., Jackson, S.N., Roux, A., Barbacci, D.C., Schultz, J.A., Balaban, C.D., Woods, A.S., 2015. Lipid imaging within the normal rat kidney using silver nanoparticles by matrix-assisted laser desorption/ionization mass spectrometry. Kidney Int. 88, 186–192.
Murphy, R.C., Hankin, J.A., Barkley, R.M., Zemski Berry, K.A., 2011. MALDI imaging of lipids after matrix sublimation/deposition. Biochim. Biophys. Acta 1811, 970–975.
Newton, J., Lima, S., Maceyka, M., Spiegel, S., 2015. Revisiting the sphingolipid rheostat: evolving concepts in cancer therapy. Exp. Cell Res. 333, 195–200.
Nielsen, M.M., Lambertsen, K.L., Clausen, B.H., Meyer, M., Bhandari, D.R., Larsen, S.T., Poulsen, S.S., Spengler, B., Janfelt, C., Hansen, H.S., 2016. Mass spectrometry imaging of biomarker lipids for phagocytosis and signalling during focal cerebral ischaemia. Sci. Rep. 6, 39571.
Ogretmen, B., 2018. Sphingolipid metabolism in cancer signalling and therapy. Nat. Rev. Cancer 18, 33–50.
Pan, N., Rao, W., Kothapalli, N.R., Liu, R., Burgett, A.W., Yang, Z., 2014. The single-probe: a miniaturized multifunctional device for single cell mass spectrometry analysis. Anal. Chem. 86, 9376–9380.
Passarelli, M.K., Pirkl, A., Moellers, R., Grinfeld, D., Kollmer, F., Havelund, R., Newman, C.F., Marshall, P.S., Arlinghaus, H., Alexander, M.R., West, A., Horning, S., Niehuis, E., Makarov, A., Dollery, C.T., Gilmore, I.S., 2017. The 3D OrbiSIMS-label-free metabolic imaging with subcellular lateral resolution and high mass-resolving power. Nat. Methods 14, 1175–1183.
Peters, R., Peters, J., Warner, J., Beckett, N., Bulpitt, C., 2008. Alcohol, dementia and cognitive decline in the elderly: a systematic review. Age Ageing 37, 505–512.
Petkovic, M., Schiller, J., Muller, M., Benard, S., Reichl, S., Arnold, K., Arnhold, J., 2001. Detection of individual phospholipids in lipid mixtures by matrix-assisted laser desorption/ionization time-of-flight mass spectrometry: phosphatidylcholine prevents the detection of further species. Anal. Biochem. 289, 202–216.
Pirro, V., Alfaro, C.M., Jarmusch, A.K., Hattab, E.M., Cohen-Gadol, A.A., Cooks, R.G., 2017. Intraoperative assessment of tumor margins during glioma resection by desorption electrospray ionization-mass spectrometry. Proc. Natl. Acad. Sci. U. S. A. 114, 6700–6705.
Pol, J., Faltyskova, H., Krasny, L., Volny, M., Vlacil, O., Hajduch, M., Lemr, K., Havlicek, V., 2015. Age-related changes in the lateral lipid distribution in a human lens described by mass spectrometry imaging. Eur. J. Mass Spectrom. (Chichester) 21, 297–303.
Popov, J., Vobornik, D., Coban, O., Keating, E., Miller, D., Francis, J., Petersen, N.O., Johnston, L.J., 2008. Chemical mapping of ceramide distribution in sphingomyelin-rich domains in monolayers. Langmuir 24, 13502–13508.
Prentice, B.M., Chumbley, C.W., Caprioli, R.M., 2016. High-speed MALDI MS/MS imaging mass spectrometry using continuous raster sampling. J. Mass Spectrom. 51, 665.
Pyne, N.J., El Buri, A., Adams, D.R., Pyne, S., 2018. Sphingosine 1-phosphate and cancer. Adv. Biol. Regul. 68, 97–106.
Qureshi, A., Subathra, M., Grey, A., Schey, K., Del Poeta, M., Luberto, C., 2010. Role of sphingomyelin synthase in controlling the antimicrobial activity of neutrophils against Cryptococcus neoformans. PLoS One 5, e15587.
Qureshi, A., Grey, A., Rose, K.L., Schey, K.L., Del Poeta, M., 2011. Cryptococcus neoformans modulates extracellular killing by neutrophils. Front. Microbiol. 2, 193.
Rao, W., Pan, N., Yang, Z., 2015. High resolution tissue imaging using the single-probe mass spectrometry under ambient conditions. J. Am. Soc. Mass Spectrom. 26, 986–993.
Rompp, A., Guenther, S., Schober, Y., Schulz, O., Takats, Z., Kummer, W., Spengler, B., 2010. Histology by mass spectrometry: label-free tissue characterization obtained from high-accuracy bioanalytical imaging. Angew. Chem. Int. Ed. Engl. 49, 3834–3838.
Roux, A., Muller, L., Jackson, S.N., Baldwin, K., Womack, V., Pagiazitis, J.G., O'Rourke, J.R., Thanos, P.K., Balaban, C., Schultz, J.A., Volkow, N.D., Woods, A.S., 2015. Chronic ethanol consumption profoundly alters regional brain ceramide and sphingomyelin content in rodents. ACS Chem. Neurosci. 6, 247–259.
Roux, A., Muller, L., Jackson, S.N., Post, J., Baldwin, K., Hoffer, B., Balaban, C.D., Barbacci, D., Schultz, J.A., Gouty, S., Cox, B.M., Woods, A.S., 2016. Mass spectrometry imaging of rat brain lipid profile changes over time following traumatic brain injury. J. Neurosci. Methods 272, 19–32.
Sans, M., Gharpure, K., Tibshirani, R., Zhang, J., Liang, L., Liu, J., Young, J.H., Dood, R.L., Sood, A.K., Eberlin, L.S., 2017. Metabolic markers and statistical prediction of serous ovarian cancer aggressiveness by ambient ionization mass spectrometry imaging. Cancer Res. 77, 2903–2913.
Schafer, K.C., Denes, J., Albrecht, K., Szaniszlo, T., Balog, J., Skoumal, R., Katona, M., Toth, M., Balogh, L., Takats, Z., 2009. In vivo, in situ tissue analysis using rapid evaporative ionization mass spectrometry. Angew. Chem. Int. Ed. Engl. 48, 8240–8242.
Schober, Y., Guenther, S., Spengler, B., Rompp, A., 2012. Single cell matrix-assisted laser desorption/ionization mass spectrometry imaging. Anal. Chem. 84, 6293–6297.
Shin, J., Berg, D.A., Zhu, Y., Shin, J.Y., Song, J., Bonaguidi, M.A., Enikolopov, G., Nauen, D.W., Christian, K.M., Ming, G.L., Song, H., 2015. Single-cell RNA-Seq with waterfall reveals molecular cascades underlying adult neurogenesis. Cell Stem Cell 17, 360–372.
Sikora, J., Dworski, S., Jones, E.E., Kamani, M.A., Micsenyi, M.C., Sawada, T., Le Faouder, P., Bertrand-Michel, J., Dupuy, A., Dunn, C.K., Xuan, I.C.Y., Casas, J., Fabrias, G., Hampson, D.R., Levade, T., Drake, R.R., Medin, J.A., Walkley, S.U., 2017. Acid ceramidase deficiency in mice results in a broad range of central nervous system abnormalities. Am. J. Pathol. 187, 864–883.
Simons, K., Ikonen, E., 1997. Functional rafts in cell membranes. Nature 387, 569–572.
Soltwisch, J., Kettling, H., Vens-Cappell, S., Wiegelmann, M., Muthing, J., Dreisewerd, K., 2015. Mass spectrometry imaging with laser-induced postionization. Science 348, 211–215.
St John, E.R., Rossi, M., Pruski, P., Darzi, A., Takats, Z., 2016. Intraoperative tissue identification by mass spectrometric technologies. Trends Analyt. Chem. 85, 2–9.
Sugimoto, M., Shimizu, Y., Yoshioka, T., Wakabayashi, M., Tanaka, Y., Higashino, K., Numata, Y., Sakai, S., Kihara, A., Igarashi, Y., Kuge, Y., 2015. Histological analyses by matrix-assisted laser desorption/ionization-imaging mass spectrometry reveal differential localization of sphingomyelin molecular species regulated by particular ceramide synthase in mouse brains. Biochim. Biophys. Acta 1851, 1554–1565.
Sugimoto, M., Wakabayashi, M., Shimizu, Y., Yoshioka, T., Higashino, K., Numata, Y., Okuda, T., Zhao, S., Sakai, S., Igarashi, Y., Kuge, Y., 2016. Imaging mass spectrometry reveals acyl-chain- and region-specific sphingolipid metabolism in the kidneys of sphingomyelin synthase 2-Deficient mice. PLoS One 11, e0152191.
Sullards, M.C., Liu, Y., Chen, Y., Merrill Jr, A.H., 2011. Analysis of mammalian sphingolipids by liquid chromatography tandem mass spectrometry (LC-MS/MS) and tissue imaging mass spectrometry (TIMS). Biochim. Biophys. Acta 1811, 838–853.
Tanaka, H., Zaima, N., Yamamoto, N., Sagara, D., Suzuki, M., Nishiyama, M., Mano, Y., Sano, M., Hayasaka, T., Goto-Inoue, N., Sasaki, T., Konno, H., Unno, N., Setou, M., 2010. Imaging mass spectrometry reveals unique lipid distribution in primary varicose veins. Eur. J. Vasc. Endovasc. Surg. 40, 657–663.
Tata, A., Woolman, M., Ventura, M., Bernards, N., Ganguly, M., Gribble, A., Shrestha, B., Bluemke, E., Ginsberg, H.J., Vitkin, A., Zheng, J., Zarrine-Afsar, A., 2016. Rapid detection of necrosis in breast Cancer with desorption electrospray ionization mass spectrometry. Sci. Rep. 6, 35374.
Tian, H., Fletcher, J.S., Thuret, R., Henderson, A., Papalopulu, N., Vickerman, J.C., Lockyer, N.P., 2014. Spatiotemporal lipid profiling during early embryo development of Xenopus laevis using dynamic ToF-SIMS imaging. J. Lipid Res. 55, 1970–1980.
Touboul, D., Brunelle, A., Laprevote, O., 2011. Mass spectrometry imaging: Towards a lipid microscope? Biochimie 93, 113–119.
Valsecchi, M., Mauri, L., Casellato, R., Prioni, S., Loberto, N., Prinetti, A., Chigorno, V., Sonnino, S., 2007. Ceramide and sphingomyelin species of fibroblasts and neurons in culture. J. Lipid Res. 48, 417–424.
van Remoortere, A., van Zeijl, R.J., van den Oever, N., Franck, J., Longuespee, R., Wisztorski, M., Salzet, M., Deelder, A.M., Fournier, I., McDonnell, L.A., 2010. MALDI imaging and profiling MS of higher mass proteins from tissue. J. Am. Soc. Mass Spectrom. 21, 1922–1929.
Vidova, V., Pol, J., Volny, M., Novak, P., Havlicek, V., Wiedmer, S.K., Holopainen, J.M.,

2010. Visualizing spatial lipid distribution in porcine lens by MALDI imaging high-resolution mass spectrometry. J. Lipid Res. 51, 2295–2302.
Walton, B.L., Verbeck, G.F., 2014. Soft-landing ion mobility of silver clusters for small-molecule matrix-assisted laser desorption ionization mass spectrometry and imaging of latent fingerprints. Anal. Chem. 86, 8114–8120.
Wang, H.Y., Wu, H.W., Tsai, P.J., Liu, C.B., 2012. MALDI-mass spectrometry imaging of desalted rat brain sections reveals ischemia-mediated changes of lipids. Anal. Bioanal. Chem. 404, 113–124.
Wang, X., Han, J., Pan, J., Borchers, C.H., 2014. Comprehensive imaging of porcine adrenal gland lipids by MALDI-FTMS using quercetin as a matrix. Anal. Chem. 86, 638–646.
Wang, S., Chen, X., Luan, H., Gao, D., Lin, S., Cai, Z., Liu, J., Liu, H., Jiang, Y., 2016. Matrix-assisted laser desorption/ionization mass spectrometry imaging of cell cultures for the lipidomic analysis of potential lipid markers in human breast cancer invasion. Rapid Commun. Mass Spectrom. 30, 533–542.
Ward, R.J., Lallemand, F., de Witte, P., 2009. Biochemical and neurotransmitter changes implicated in alcohol-induced brain damage in chronic or' binge drinking' alcohol abuse. Alcohol Alcohol. 44, 128–135.
Williams, P., 2006. Biological imaging using secondary ions. J. Biol. 5, 18.
Wilson, R.L., Kraft, M.L., 2013. Quantifying the molar percentages of cholesterol in supported lipid membranes by time-of-flight secondary ion mass spectrometry and multivariate analysis. Anal. Chem. 85, 91–97.
Wiseman, J.M., Li, J.B., 2010. Elution, partial separation, and identification of lipids directly from tissue slices on planar chromatography media by desorption electrospray ionization mass spectrometry. Anal. Chem. 82, 8866–8874.
Wiseman, J.M., Puolitaival, S.M., Takats, Z., Cooks, R.G., Caprioli, R.M., 2005. Mass spectrometric profiling of intact biological tissue by using desorption electrospray ionization. Angew. Chem. Int. Ed. Engl. 44, 7094–7097.
Wojakowska, A., Cole, L.M., Chekan, M., Bednarczyk, K., Maksymiak, M., Oczko-Wojciechowska, M., Jarzab, B., Clench, M.R., Polanska, J., Pietrowska, M., Widlak, P., 2018. Discrimination of papillary thyroid cancer from non-cancerous thyroid tissue based on lipid profiling by mass spectrometry imaging. Endokrynol. Pol. 69, 2–8.
Wolstenholme, R., Bradshaw, R., Clench, M.R., Francese, S., 2009. Study of latent fingermarks by matrix-assisted laser desorption/ionisation mass spectrometry imaging of endogenous lipids. Rapid Commun. Mass Spectrom. 23, 3031–3039.
Woods, A.S., Colsch, B., Jackson, S.N., Post, J., Baldwin, K., Roux, A., Hoffer, B., Cox, B.M., Hoffer, M., Rubovitch, V., Pick, C.G., Schultz, J.A., Balaban, C., 2013. Gangliosides and ceramides change in a mouse model of blast induced traumatic brain injury. ACS Chem. Neurosci. 4, 594–600.
Wu, C., Ifa, D.R., Manicke, N.E., Cooks, R.G., 2010. Molecular imaging of adrenal gland by desorption electrospray ionization mass spectrometry. Analyst 135, 28–32.
Xu, C., Zhou, D., Luo, Y., Guo, S., Wang, T., Liu, J., Liu, Y., Li, Z., 2017. Tissue and serum lipidome shows altered lipid composition with diagnostic potential in mycosis fungoides. Oncotarget 8, 48041–48050.
Yamashita, R., Tabata, Y., Iga, E., Nakao, M., Sano, S., Kogure, K., Tokumura, A., Tanaka, T., 2016. Analysis of molecular species profiles of Ceramide-1-phosphate and sphingomyelin using MALDI-TOF mass spectrometry. Lipids 51, 263–270.
Yamazaki, K., Masaki, N., Kohmura-Kobayashi, Y., Yaguchi, C., Hayasaka, T., Itoh, H., Setou, M., Kanayama, N., 2015. Decrease in Sphingomyelin (d18:1/16:0) in stem villi and phosphatidylcholine (16:0/20:4) in terminal villi of human term placentas with pathohistological maternal malperfusion. PLoS One 10, e0142609.
Yang, J., Caprioli, R.M., 2013. Matrix precoated targets for direct lipid analysis and imaging of tissue. Anal. Chem. 85, 2907–2912.
Yeager, A.N., Weber, P.K., Kraft, M.L., 2016. Three-dimensional imaging of cholesterol and sphingolipids within a Madin-Darby canine kidney cell. Biointerphases 11, 02A309.
Zaima, N., Goto-Inoue, N., Adachi, K., Setou, M., 2011. Selective analysis of lipids by thin-layer chromatography blot matrix-assisted laser desorption/ionization imaging mass spectrometry. J. Oleo Sci. 60, 93–98.
Zavalin, A., Yang, J., Haase, A., Holle, A., Caprioli, R., 2014. Implementation of a Gaussian beam laser and aspheric optics for high spatial resolution MALDI imaging MS. J. Am. Soc. Mass Spectrom. 25, 1079–1082.
Zavalin, A., Yang, J., Hayden, K., Vestal, M., Caprioli, R.M., 2015. Tissue protein imaging at 1 mum laser spot diameter for high spatial resolution and high imaging speed using transmission geometry MALDI TOF MS. Anal. Bioanal. Chem. 407, 2337–2342.
Zhang, Y., Li, X., Becker, K.A., Gulbins, E., 2009. Ceramide-enriched membrane domains–structure and function. Biochim. Biophys. Acta 1788, 178–183.
Zhang, J., Feider, C.L., Nagi, C., Yu, W., Carter, S.A., Suliburk, J., Cao, H.S.T., Eberlin, L.S., 2017. Detection of metastatic breast and thyroid cancer in lymph nodes by desorption electrospray ionization mass spectrometry imaging. J. Am. Soc. Mass Spectrom. 28, 1166–1174.
Zhao, C., Xie, P., Yong, T., Wang, H., Chung, A.C.K., Cai, Z., 2018. MALDI-MS imaging reveals asymmetric spatial distribution of lipid metabolites from bisphenol S-Induced nephrotoxicity. Anal. Chem. 90, 3196–3204.
Zheng, L., McQuaw, C.M., Ewing, A.G., Winograd, N., 2007. Sphingomyelin/phosphatidylcholine and cholesterol interactions studied by imaging mass spectrometry. J. Am. Chem. Soc. 129, 15730–15731.